Title

Dissecting the molecular mechanisms of cell division: A novel methylation equilibrium regulates spindle size in mitotic cells and Multidisciplinary high-throughput screening to discover novel anti-leukemia small molecule drugs

Author

Xia, Xiaoyu

Publication Date

2015

Peer reviewed|Thesis/dissertation

UNIVERSITY OF CALIFORNIA

Los Angeles

Dissecting the molecular mechanism of cell division:

A novel methylation equilibrium regulates the spindle size in mitotic cells

and Multidisciplinary high-throughput screening to discover novel anti-leukemia small molecule drugs

A Dissertation submitted in partial satisfaction of the requirements for the degree

Doctor of Philosophy

in Biochemistry and Molecular Biology

by

Xiaoyu Xia

2015

ABSTRACT OF THE DISSERTATION

Dissecting the molecular mechanism of cell division: A novel methylation equilibrium regulates the spindle size in mitotic cells and Multidisciplinary high-throughput screening to discover novel anti-leukemia small molecule drugs

by

Xiaoyu Xia

Doctor of Philosophy in Biochemistry and Molecular Biology

University of California, Los Angeles

Professor Jorge Z. Torres, Chair

Mitotic spindle assembly is a highly complex and specifically orchestrated event that occurs once per cell division. It relies on a multitude of protein complexes, protein-protein interactions, and regulatory mechanisms. To date, many proteins that associate with microtubules and function in mitotic spindle assembly have been identified and characterized. A strategy in the treatment of cancer has been to inhibit cell division with antimitotics, a group of natural and synthetic small molecules that arrest cells in mitosis, induce apoptosis, and cause cell death. My research focuses on finding potential cancer therapeutics by identifying novel

antimitotic proteins, and by developing anti-leukemia small molecule drugs.

Leucine carboxyl methyltransferase-1 (LCMT1) and protein phosphatase methylesterase-1 (PME-1) are essential enzymes that regulate the methylation of the protein phosphatase 2A catalytic subunit (PP2AC). LCMT1 and PME-1 have been linked to regulating cell growth and proliferation, but the underlying mechanisms have remained elusive. We show here an important role for an LCMT1-PME-1 methylation equilibrium in controlling mitotic spindle size. Depletion of LCMT1 or overexpression of PME-1 led to long spindles. In contrast, depletion of PME-1, pharmacological inhibition of PME-1 or overexpression of LCMT1 led to short spindles. Furthermore, perturbation of the LCMT1-PME-1 methylation equilibrium led to defective cell divisions, induction of apoptosis and reduced cell viability. Thus, we propose that the LCMT1-PME-1 methylation equilibrium is critical for regulating mitotic spindle size and thereby proper cell division.

Targeting of the leukemia proliferation cycle has been a successful approach to developing antileukemic therapies. However, drug-screening efforts to identify novel anti-leukemia agents have been hampered by the lack of a suitable high-throughput screening platform for suspension cells that does not rely on FACS analyses. We report the development of a novel leukemia cell-based high-throughput chemical screening platform for the discovery of cell cycle phase specific inhibitors that relies on the use of chemical cell cycle profiling. We have used this approach to analyze the cell cycle response of leukemia CCRF-CEM cells to each of 181,420 drug-like compounds. This approach yielded cell cycle phase specific inhibitors of leukemia cell proliferation. Further analyses of the top G2-phase and M-phase inhibitors

identified a leukemia specific inhibitors (Leusin-1). Leusin-1 arrests cells in G2-phase and trigger an apoptotic cell death. More importantly, Leusin-1 was more active in acute lymphoblastic leukemia cells than other types of leukemia, non blood-born cancers, or normal cells. Leusin-1 represents novel leukemia specific inhibitors and could be used to develop new anti-leukemia therapies.

The dissertation of Xiaoyu Xia is approved.

Steven G. Clarke

James A. Wohlschlegel

Jorge Z. Torres, Committee Chair

University of California, Los Angeles

2015

Dedicated to my grandma.

TABLE OF CONTENTS

List of Figures

A LCMT1-PME-1 Methylation Equilibrium Controls Mitotic Spindle Size

List of Supplemental Tables and Figures

Pharmacological Inhibition of the Leukemia Cell Cycle Identifies Specific Inhibitors of Leukemia Cell Proliferation

ABBREVIATIONS

ALL	Acute lymphoblastic leukemia
AML	Acute Myeloid Leukemia
AMZ-30	PME-1 specific inhibitor
APC/C	Anaphase promoting complex/cyclosome
ATP	Adenosine triphosphate
BAZ2a	Bromodomain adjacent to zinc finger domain 2A
BAZ2b	Bromodomain adjacent to zinc finger domain 2B
BCL-2	B-cell lymphoma 2
BCL-XL	B-cell lymphoma-extra large
Bub1	Budding uninhibited by benzimidazoles 1**,** SAC kinase
Cdc27	Cell division cycle protein 27
CHOP	Encodes for DNA damage-inducible transcript 3
CML	Chronic Myeloid Leukemia
CNS	Central nervous system
DAPI	4', 6-diamidino-2-phenylindole
DARTS	Drug affinity response target stability
DD	Defective division
DM	Death in mitosis
DMSO	Dimethyl sulfoxide
Dox	Doxycycline
EDEM	Encodes for ER degradation enhancer, mannosidase alpha-like 1
FDA	Federal drug administration

GAPDH	Glyceraldehyde 3-phosphate dehydrogenase
HSPA	Encodes for heat shock protein A
IC_{50}	Half maximal inhibitory concentration
ITC	Isothermal titration calorimetry
LAP	Localization and affinity purification
LCMT1	Leusine carboxyl methyltransferase-1
MA	Mitotic arrest
NOC	Nocodazole
NoRC	Nucleolar remodeling complex
OE	Overexpression
p-H3	Phospho-Histone 3
Peri	Pericentrin
pH2AX	Phosphorylated H2A histone family, member X
PME-1	Protein phosphatase methylesterase-1
PP2A	Protein phosphatase 2A
PP2AC	Catalytic subunit of protein phosphatase 2A
PTP	Spindle pole-to-pole
R&D	Research and development
SAC	Spindle assembly checkpoint
SAH	S-adenosyl-L-homocysteine
SAM	S-Adenosyl-L-Methionine
shRNA	Short hairpin RNA
siRNA	Small interfering RNA
TAP	Tandem affinity purification

Tau	Protein that stabilizes microtubules
UPR	Unfolded protein response
XBP-1	X-box binding protein 1
XBP-1s	X-box binding protein 1 spliced
XBP-1u	X-box binding protein 1 unspliced
XMAP215	Microtubule-associated proteins
α-Tub	α-Tubulin

ACKNOWLEDGEMENTS

I would like to acknowledge my advisor and my co-authors on the works presented in this dissertation. First, I would like to thank my advisor, Dr. Jorge Torres, for giving me the financial and intellectual support to conduct my work. Second, I would like to extend my gratitude to the entire Torres lab. Ankur Gholkar, Silvia Senese, Keith Cheung, Ben Lo, for collaboration on my work. To my friends in the lab, thank you for all the scientific, academic, personal and career advises, for your supports when I feel down, and cheers for my success. To all the past members of Torres Lab, Melissa Chavez, James Deardorff, Harish Dharmarajan, Lisa, Emmanuel Hodara, Ely Contreras, wish your all the best on your future career.

I would also like to thank Dr. Courey and Dr. Koehler for the opportunity to rotate in your labs in my first year. To the members of Courey and Koehler lab, Wiam Turki-Judeh, Joseph Cao, Dennis Kuo, Alberto Ponce, Michael Chambers, Juwina Wijaya, and Sam Hasson, , thank you for your mentorship and always willing to help me.

Thanks to my committee members, Dr. Steven Clarke, Dr. Catherine Clarke, Dr. James Wohlschlegel, and Dr. Timothy Lane, for meeting with me every year and giving me feedbacks on my work.

My graduate education wouldn't be possible without my past mentors, Dr. Richard Davis, Dr. Seema Tiwari-Woodruff, and Dr. Vivek Bhalla, thank you for the opportunity to work with you and learn, and all the encouragements I received to pursue my passion in science and led me to where I am today.

I am fortunate to have met all the great people during my graduate school, including my colleagues who I studied with, professors I took class with and I TAed for, facility personnel

who gave me tremendous help when I needed them (especially Matthew Graf and Martin Phillips). Thank you for keep my graduate life educative, diverse and fun. Wish you all success and happiness.

Last but not least, this long journey couldn't be completed without the support of my family. Mom, dad, and Jia, thank you for giving me the freedom to pursue my dream, to always be there when I needed you, and all the sacrifices you made to give me the best of everything.

The research in Chapter 1-4 was originally published in the Cell Cycle: Xia X, Gholkar AA, Senese S, Torres JZ. "A LCMT1-PME-1 Methylation Equilibrium Controls Mitotic Spindle Size." Cell Cycle. 2015;14(12):1938-47.

The research project "A LCMT1-PME-1 Methylation Equilibrium Controls Mitotic Spindle Size" is supported by the National Science Foundation under Grant Number MCB1243645, awarded to Jorge Z. Torres. The research project "Pharmacological Inhibition of the Leukemia Cell Cycle Identifies Specific Inhibitors of Leukemia Cell Proliferation" is supported by the National Cancer Institute of the National Institutes of Health under award number P30CA016042, granted to the Molecular Screening Shared Resource. This work was also supported by a Jonsson Cancer Center Foundation seed grant, The V Foundation for Cancer Research V Scholar Award and University of California Cancer Research Coordinating Committee Funds, awarded to Jorge Z. Torres.

CURRICULUM VITAE

Xiaoyu Xia

EDUCATION

Bachelor of Science **2004- 2006**
University of California, Los Angeles
Department of Chemistry and Biochemistry

HONORS & AWARDS

University Fellowship **2009**
Department of Chemistry and Biochemistry
University of California, Los Angeles

Dean's Honor List **2005**
Department of Chemistry and Biochemistry
University of California, Los Angeles

RESEARCH EXPERIENCE

Lab Manager, Bhalla Lab, Stanford University **2008 - 2009**
Project 1: Inhibition of Epithelial Na^+ Channel by novel phosphorylation sites of Nedd4-2
Project 2: Map glomerular gene expression profiles in diabetic murine models that resemble early stages of human diabetic nephropathy

Research Associate, Tiwari-Woodruff Lab, UCLA **2006 - 2007**
Project 1:Recovery analysis of Corpus Callosum following demyelination
Project 2: Characterization of chronic experimental autoimmune encephalomyelitis (EAE) mouse model of cortical and callosal pathology in multiple sclerosis

Undergraduate Training, Lusis Lab, UCLA **2004-2006**
Undergraduate Research Project 1: Investigation of the role of Abcc6 gene, relationship between Abcc6 with heart calcification
Undergraduate Research Project 2: A genome-wide set of congenic mouse strains derived from CAST/Ei on a C57BL/6 background

TEACHING EXPERIENCE

Biochemistry 153L "Biochemical Methods I" **2014F**
Teaching Assistant for Dr. Anne Hong-Hermesdorf

Chemistry 20L "General Chemistry Lab" **2014W**

Teaching Assistant for Dr. Johnny Pang

Biochemistry C165/C265 "Metabolic Control by Protein Modification" **2013S, 2012S**
Teaching Assistant for Dr. Jorge Torres

Biochemistry153C "Metabolism and Regulation" **2010S**
Teaching Assistant for Dr. Richard Weiss

Biochemistry 153C "Metabolism and Regulation" **2010W**
Teaching Assistant for Dr. James Gober

PUBLICATIONS

Xia X, Gholkar AA, Senese S, Torres JZ. "A LCMT1-PME-1 Methylation Equilibrium Controls Mitotic Spindle Size." *Cell Cycle.* 2015;14(12):1938-47

Senese S, Cheung K, Lo YC, Gholkar AA, **Xia X**, Wohlschlegel JA, Torres JZ. "A Unique Insertion in STARD9's Motor Domain Regulates Its Stability; Critical for Cell Division." *Mol Biol Cell.* 2015 Feb 1;26(3):440-52.

Mangiardi M, Crawford DK, **Xia X**, Du S, Simon-Freeman R, Voskuhl RR, Tiwari-Woodruff SK. "An animal model of cortical and callosal pathology in multiple sclerosis." *Brain Pathol.* 2011 May;21(3):263-78.

Hallows KR, Bhalla V, Oyster NM, Wijngaarden MA, Lee JK, Li H, Chandran S, **Xia X**, Huang Z, Chalkley RJ, Burlingame AL, Pearce D. "Phosphopeptide screen uncovers novel phosphorylation sites of Nedd4-2 that potentiate its inhibition of the epithelial Na+ channel." *J Biol Chem*. 2010 Jul 9;285(28):21671-8.

Crawford DK, Mangiardi M, **Xia X**, López-Valdés HE, Tiwari-Woodruff SK. "Functional recovery of callosal axons following demyelination: a critical window." *Neuroscience*. 2009 Dec 29;164(4):1407-21.

Davis RC, Jin A, Rosales M, Yu S, **Xia X**, Ranola K, Schadt EE, Lusis AJ. "A genome-wide set of congenic mouse strains derived from CAST/Ei on a C57BL/6 background." *Genomics*. 2007 Sep;90(3):306-13.

CONFERENCES

American Society for Cell Biology Annual Meeting **San Francisco, 2012**

Society of Neuroscience Conference **San Diego, 2007**
Poster Presentation "Corpus callosum of EAE and cuprizone-induced demyelinating mice show similar conduction deficit and pathology"

A LCMT1-PME-1 Methylation Equilibrium Controls Mitotic Spindle Size

CHAPTER 1 - INTRODUCTION

Leucine carboxyl methyltransferase-1 (LCMT1) is a monomeric 38-kDa protein that catalyzes the transfer of methyl groups from S-Adenosyl-L-Methionine (SAM) to the α-carboxyl leucine of the catalytic subunit of protein phosphatase 2A (PP2AC).[1] The PP2A phosphatase has established roles in cell signaling and cell proliferation and is composed of a scaffold subunit (A subunit), a catalytic subunit (C subunit), and one of many regulatory subunits (B, B', B'', B''' subunits) that provide substrate specificity and generate >60 PP2A holoenzymes.[2, 3] Methylation of PP2AC controls its association with specific regulatory subunits (B subunits), thus modulating PP2A activity towards specific substrates.[2, 4] This methylation is reversible by the protein phosphatase methylesterase-1 (PME-1).[5, 6] Outside of PP2AC, there are no known substrates of LCMT1 or PME-1, thus it has been hypothesized that the main role of these enzymes is to regulate the abundance of specific PP2A holoenzymes. Interestingly, homozygous deletion of either LCMT1 or PME-1 in mice is embryonic lethal, indicating that their role in regulating PP2A through methylation/demethylation is critical for cell growth and development.[7, 8]

A recent report demonstrated that depletion of LCMT1 led to an abnormal progression through mitosis and an increase in cell death[7], thus implicating LCMT1 in the regulation of normal cell division and survival. However, the mechanism of how LCMT1 functions to promote proper cell division has remained elusive. As PME-1 counteracts LCMT1 methylation activity, it is reasonable to postulate that PME-1 might also have a role in regulating cell division. However, this hypothesis has also remained unexplored. In this study, we have analyzed the role of LCMT1 and PME-1 in cell division. Surprisingly, we uncovered a

previously undescribed methylation equilibrium established by LCMT1 and PME-1 that is critical for regulating mitotic spindle size and its misregulation leads to defective cell divisions and reduced cell viability.

CHAPTER 2 - RESULTS

2.1 Perturbation of the LCMT1-PME-1 methylation equilibrium leads to an abnormal mitotic spindle size

To define the role of LCMT1 in cell division and to determine if PME-1 was necessary for normal cell division, we analyzed the cellular consequences of depleting LCMT1 and PME-1. First, we verified that siRNA oligonucleotides targeting LCMT1 (siLCMT1) and PME-1 (siPME-1) were able to deplete LCMT1 and PME-1 protein levels compared to non-targeting siRNAs (siControl) (**Fig. 2.1.1**).

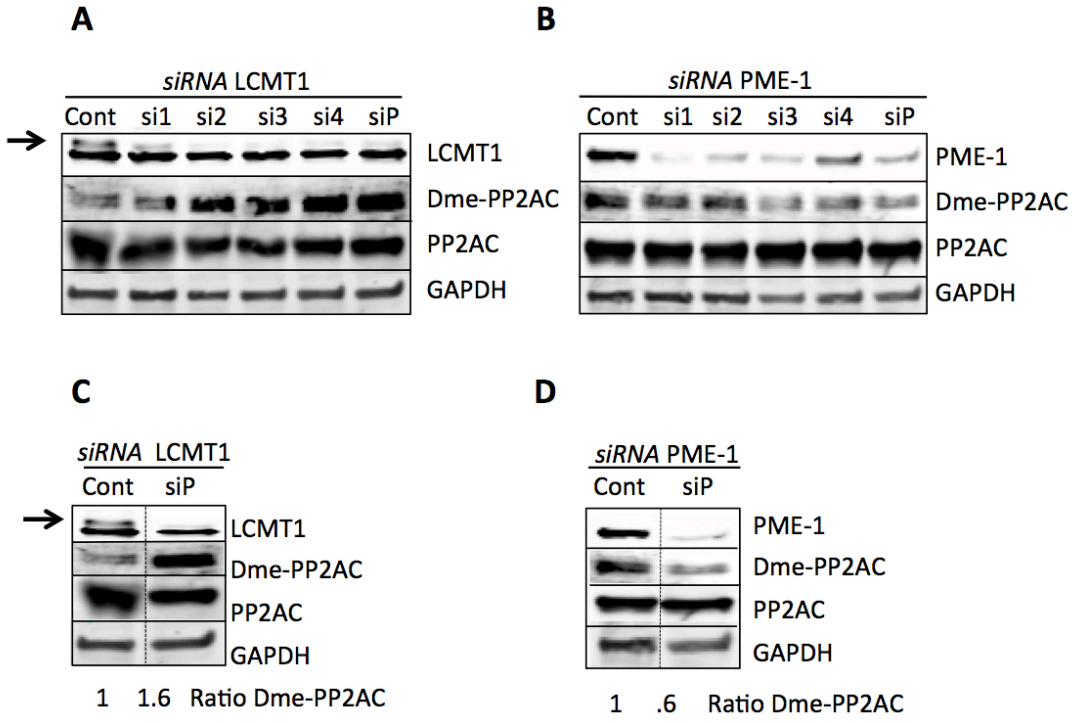

Figure 2.1.1 - siRNA mediated depletion of LCMT1 and PME-1. (**A-B**) HeLa cells were treated with siRNAs targeting LCMT1 (**A**) or PME-1 (**B**) for 48 hours and protein extracts were analyzed by immunoblotting with the indicated antibodies. Cont = control non-targeting siRNA, si1-si4 indicate individual oligos and siP indicates pooled oligos. (**C-D**) siRNA knockdown of LCMT1 (**C**) or PME-1 (**D**) expression levels compared to control non-targeting siRNA. Note that the levels of demethylated PP2AC decreases in PME-1 depleted cells and increases in LCMT1 depleted cells.

Human HeLa cells were then transfected with siControl, siLCMT1, or siPME-1 for 48 hours. Cells were fixed, costained for DNA, α-tubulin and Pericentrin, and imaged by fluorescence microscopy (**Fig. 2.1.2A**). Interestingly, depletion of LCMT1 led to abnormally long spindles with spindle multipolarity and aberrant unaligned chromosomes (**Fig. 2.1.2A-B**). Conversely, depletion of PME-1 led to abnormally short spindles and chromosomes not fully aligned at the metaphase plate (**Fig. 2.1.2B**). Quantitative analysis of these data showed that depletion of both LCMT1 and PME-1 led to a major increase in the percentage of mitotic cells (siLCMT1= 33.6±3.7 (p=0.0011) and siPME-1= 30.3±6.0 (p=0.033) compared to siControl= 8.7±1.7), aberrant mitotic spindles (predominantly long spindles = 27.7±2.1 (p=0.0008) and multipolar spindles= 30.3±2.0 (p=0.0014) compared to siControl= 4.3±1.2 and 9.7±1.7 respectively for siLCMT1 and short spindles for siPME-1= 41.3±2.9 (p=0.0001) compared to siControl= 4.6±0.9) and an increase in the percentage of cells with unaligned chromosomes (siLCMT1= 53±5.1 (p=0.0027) and siPME-1= 51±2.2 (p=0.0001) compared to siControl= 7±2.2) (**Fig. 2.1.2C-E**).

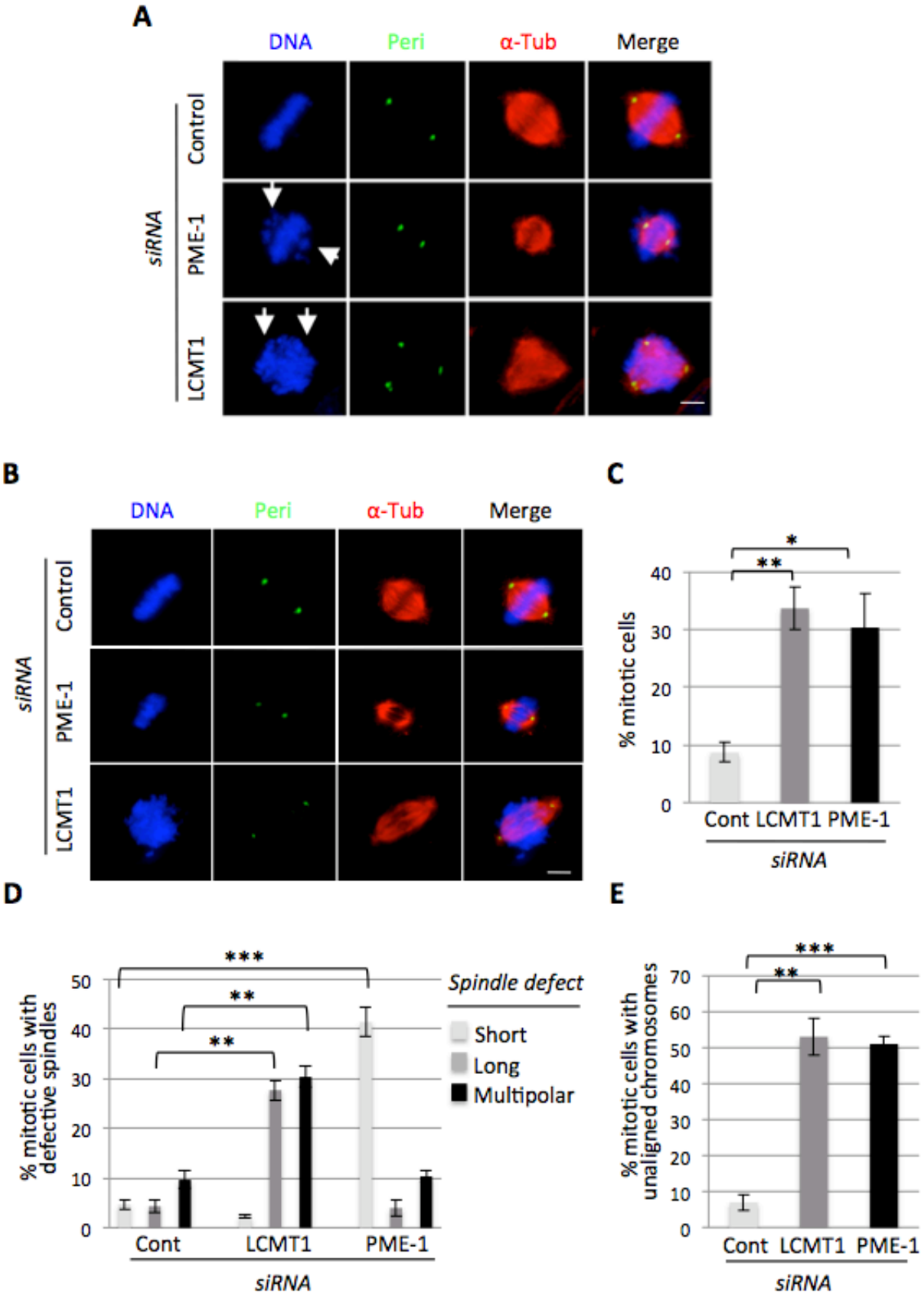
A
DNA
Peri
α-Tub
Merge
siRNA
Control
PME-1
LCMT1
B
DNA
Peri
α-Tub
Merge
siRNA
Control
PME-1
LCMT1
C
% mitotic cells
0
10
20
30
40
*
**
Cont
LCMT1
PME-1
siRNA
D
% mitotic cells with defective spindles
0
10
20
30
40
50
***
**
**
Cont
LCMT1
PME-1
siRNA
Spindle defect
Short
Long
Multipolar
E
% mitotic cells with unaligned chromosomes
0
10
20
30
40
50
60
70
***
**
Cont
LCMT1
PME-1
siRNA

Figure 2.1.2 - Spindle assembly defects of cells with a perturbed LCMT1-PME-1 methylation equilibrium. (**A**) Immunofluorescence microscopy of cells with indicated treatments stained for DNA (Hoechst 33342), α-tubulin (anti-α-tubulin antibodies) and Pericentrin (anti-pericentrin antibodies). LCMT1 depletion by siRNA leads to long multipolar or fragmented spindles with unaligned chromosomes, while depletion of PME-1 by siRNA leads to short spindles with unaligned chromosomes (see white arrows). Bar=5μm. (**B**) Immunofluorescence microcopy showing that PME-1 depletion leads to abnormally short spindles and LCMT1 depletion leads to abnormally long spindles. Bar= 5μm. (**C**) Quantification of the percentage of cells in mitosis showing that depletion of LCMT1 or PME-1 leads to a major increase in cells arrested in mitosis. (**D**) Quantification of the percentage of mitotic cells with abnormal spindles (short, long, multipolar) showing that depletion of LCMT1 or PME-1 leads to a major increase in abnormal spindles. (**E**) Quantification of the percentage of mitotic cells with unaligned chromosomes showing that depletion of LCMT1 or PME-1 leads to a major increase in unaligned chromosomes. (**C, D, E)** Data represents average ± SDs of three independent experiments. *=P< 0.05, **=P<0.005, ***=P<0.0005, ns= not statistically significant.

Since depletion of LCMT1 and PME-1 appeared to have opposing effects on spindle length, we measured the pole-to-pole (PTP) distance of siControl, siLCMT1 or siPME-1 metaphase spindles (**Fig. 2.1.3A-B)** siControl cells had a PTP distance of 11.2μm±.45, whereas siLCMT1 metaphase spindles were longer (13.8μm±.49, p=0.0056) and those of siPME-1 were shorter (7.5μm±.32, p=0.0041) (**Fig. 2.1.3B**). However, siLCMT1 cells had a similar spindle width (8.9μm±.15) to siControl cells (8.9μm±.24), whereas the spindle width of siPME-1 cells was shorter (5.6μm±.3, p=0.0007) (**Fig. 2.1.3C**). Nonetheless, the total spindle volume was abnormally large for siLCMT1 mitotic spindles (569.7μm^3±38.7, p=0.0366) and abnormally small for siPME-1 mitotic spindles (125.7μm^3±14.9, p=0.0024), compared to siControl mitotic spindles (466.3μm^3±38.8) (**Fig. 2.1.3D**). These data indicated that LCMT1 and PME-1 were indeed regulating mitotic spindle size. Consistently, there was also a reduction in the total fluorescence intensity of spindle microtubules for siLCTM1 (606 A.U.±34, p=0.025) and siPME-1 (253 A.U.±50, p=0.049) compared to siControl (434 A.U.±37) (**Fig. 2.1.3E**). Together,

these results indicated that a balance between LCMT1 methylation and PME-1 demethylation was responsible for regulating spindle size, potentially through the modulation of PP2AC methylation (**Fig. 2.1.3G**). In support of this idea, siLCMT1 led to an increase in the ratio of demethylated PP2AC (siControl=1±.3, siLCMT1=1.6±.07) whereas siPME-1 led to a decrease in the ratio of demethylated PP2AC (siControl=1±.12, siPME-1= 0.6±.13), consistent with previous reports (**Fig. 2.1.1A-B**).[4, 9]

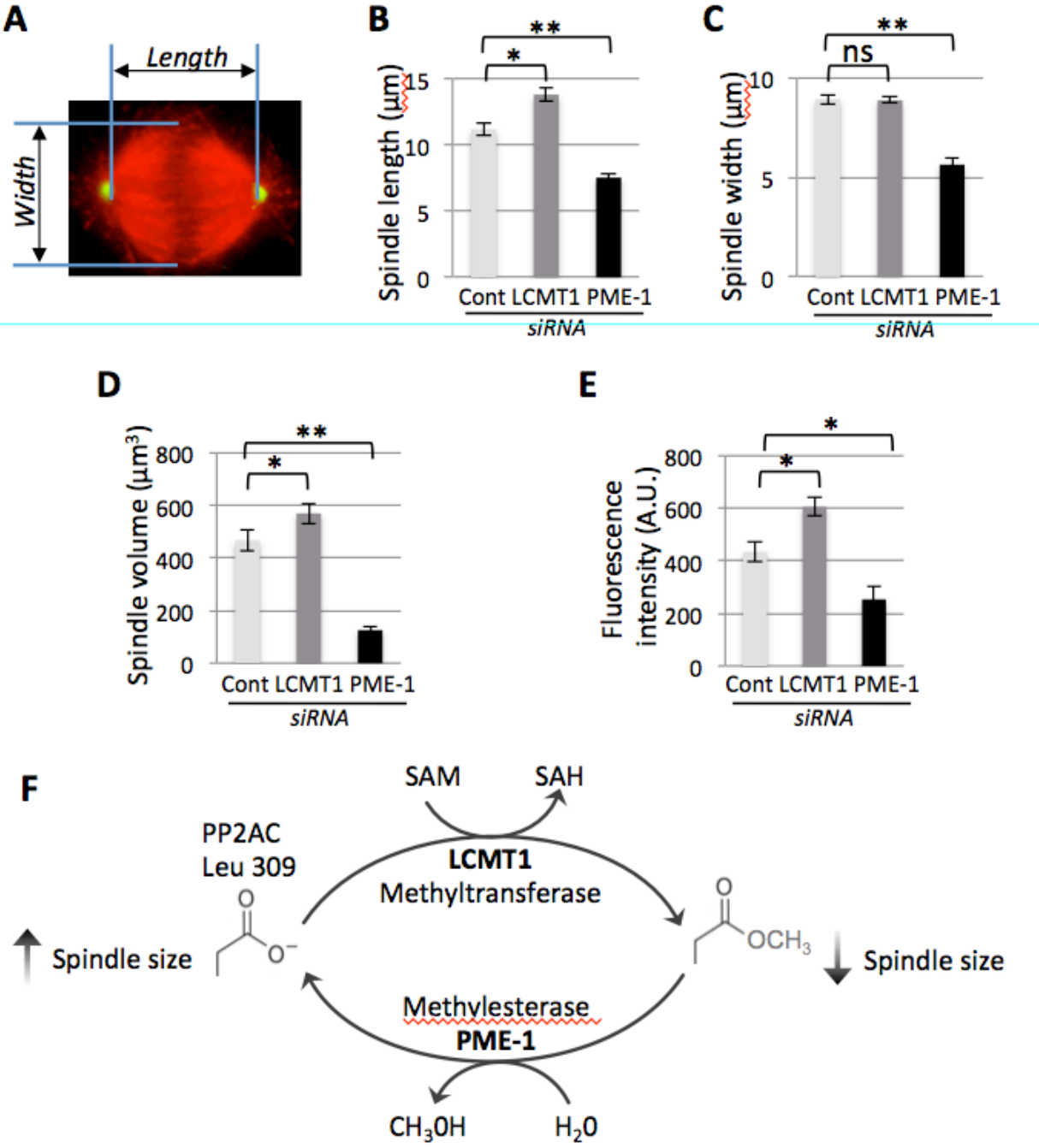

Figure 2.1.3 – Perturbation of LCMT1-PME-1 methylation equilibrium by silencing leads to abnormal mitotic spindle size. (**A**) Outline of metaphase spindle pole-to-pole (PTP) distance and width measurements. (**B**) Quantification of metaphase spindle PTP distance (in µm) showing that depletion of PME-1 leads to abnormally short spindles and depletion of LCMT1 depletion leads to abnormally long spindles. (**C**) Quantification of metaphase spindle width (in µm) showing that depletion of PME-1 leads to abnormally short spindle widths, while depletion of LCMT1 had no significant effect on spindle width. (**D**) Quantification of metaphase spindle volume (in μm^3) showing that depletion of PME-1 leads to a decrease in volume and depletion of

LCMT1 leads to an increase in volume. (**E**) Quantification of the total fluorescence intensity of mitotic spindle microtubules for PME-1 or LCMT1-depleted cells, in arbitrary units (A.U.), showing that depletion of PME-1 or LCMT1 leads to a decrease in total microtubules. (**F**) Model of the LCMT1-PME-1 methylation equilibrium that regulates spindle size and normal cell division. (**B**, **C, D, E)** Data represents average ± SDs of three independent experiments. *=P< 0.05, **=P<0.005, ***=P<0.0005, ns= not statistically significant.

2.2 Pharmacological inhibition of PME-1 leads to short mitotic spindles

Due to the recent availability of a PME-1 specific inhibitor (AMZ30) [10, 11], we sought to further test this hypothesis through pharmacological inhibition of PME-1. HeLa cells were synchronized in G1/S and released into the cell cycle in the presence of control DMSO or AMZ30 for 9 hours and then processed for quantitative immunofluorescence analyses of spindle morphology, size, width, and volume as described above. Consistent with our previous results with siRNA-mediated depletion of PME-1, treatment of cells with AMZ30 led to a decrease in the ration of demethylated PP2AC (Control=1±.06, AMZ30=0.3±.01) (**Fig. 2.2.1A**), an increase in the percentage of cells arrested in mitosis (46±3.7, p=0.001) compared to DMSO (10±2.2) (**Fig. 2.2.1C-D)**, an increase in the percentage of mitotic cells with spindle defects (predominantly abnormally small metaphase spindles (61.3±6.6, p=0.0003) compared to DMSO (6.0±1.6)) (**Fig. 2.2.1C, E**), an increase in the percentage of cells with unaligned chromosomes (78±5.4, p=0.0001) compared to DMSO (12±2.2) (**Fig. 2.2.1B, F**).

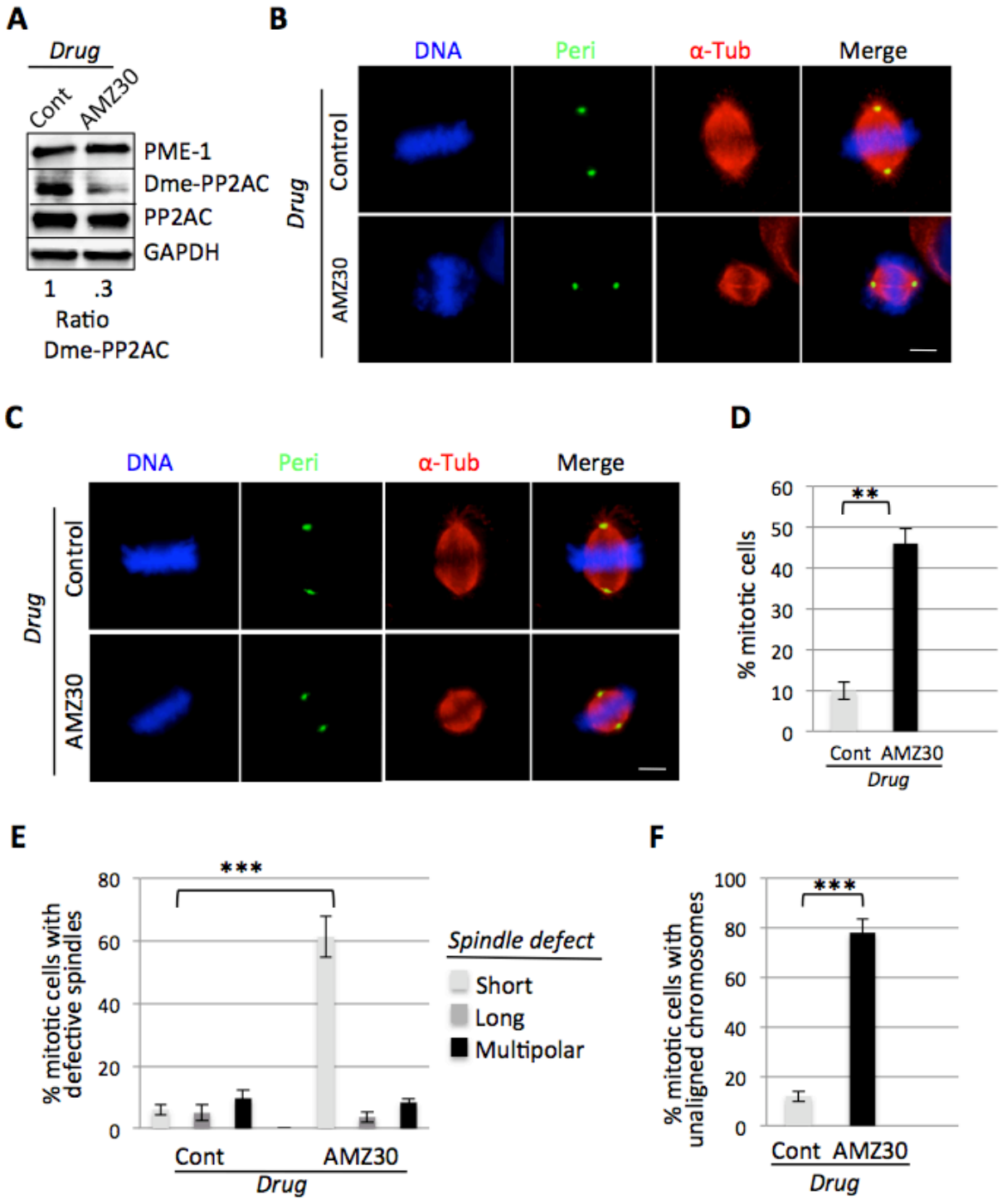

Figure 2.2.1 - Pharmacological-mediated perturbation of the LCMT1-PME-1 methylation equilibrium leads to spindle assembly defects. (**A**) Pharmacological inhibition of PME-1 with AMZ30 compared to DMSO vehicle control. Note that the levels of demethylated PP2AC decreased in cells treated with AMZ30. (**B**) Immunofluorescence microscopy of cells with

indicated treatments stained for DNA (Hoechst 33342), α-tubulin (anti-α-tubulin antibodies) and Pericentrin (anti-pericentrin antibodies). Pharmacological inhibition of PME-1 with AMZ-30 leads to short spindles with unaligned chromosomes (see white arrows) (**C**) Immunofluorescence microcopy showing that AMZ30-treated cells have abnormally short spindles. Bar= 5μm. (**D**) Quantification of the percentage of cells in mitosis showing that inhibition of PME-1 with AMZ30 leads to a major increase in cells arrested in mitosis. (**E**) Quantification showing that treatment of cells with AMZ30 leads to a major increase in the percentage of mitotic cells with abnormal spindles (short, long, multipolar). (**F**) Quantification showing that treatment of cells with AMZ30 leads to a major increase in the percentage of unaligned chromosomes. (**D-F**) Data represents average ± SDs of three independent experiments. **=P<0.005, ***=P<0.0005.

In addition, pharmacological inhibition of PME-1 by AMZ-30 results in a reduced PTP distance (6.1μm±.49, p=0.014) compared to DMSO (10.9μm±.42) (**Fig. 2.2.2A**), a reduced spindle width (6.7μm±.17, p=0.0009) compared to DMSO (8.4μm±.02) (**Fig. 2.2.2B**), a reduced spindle volume (121μm^3±40, p=0.0006) compared to DMSO (400.1μm^3±16.5) (**Fig. 2.2.2C**), a reduction in the total fluorescence intensity of spindle microtubules (247 A.U.±42, p=0.027) compared to DMSO (418 A.U.±57) (**Fig. 2.2.2D**). Therefore, the results of inhibiting PME-1 pharmacologically were consistent with the results of depleting PME-1 and further supported the hypothesis that misregulation of the LCMT1-PME-1 methylation equilibrium led to an abnormal spindle size.

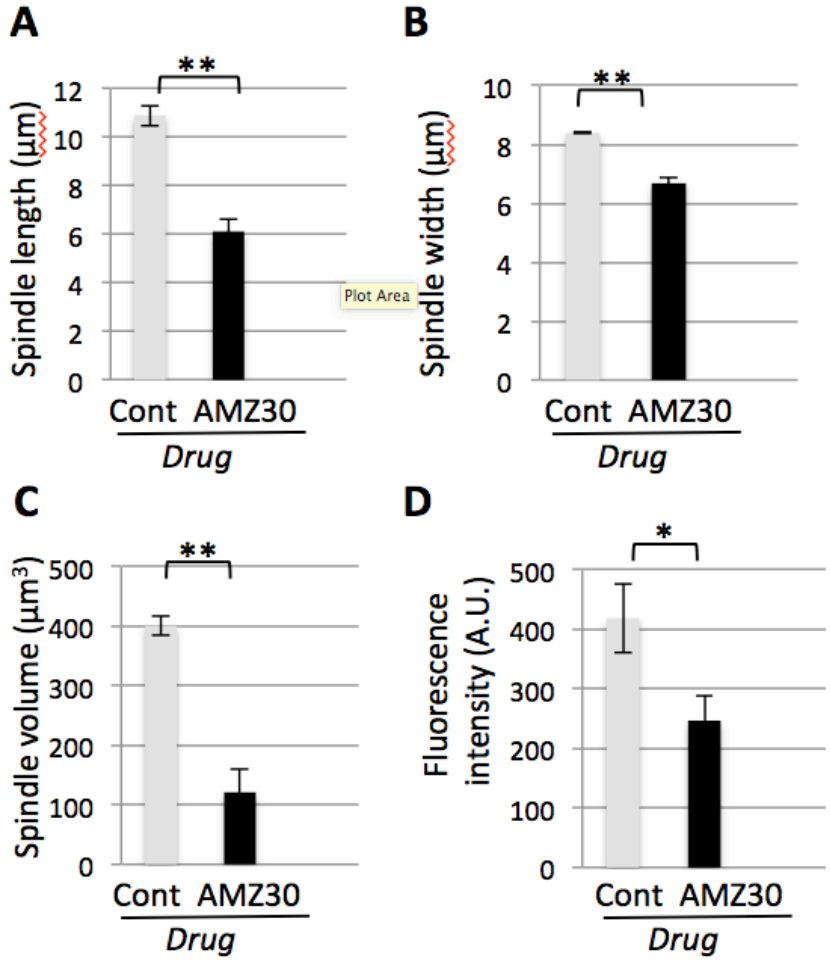

Figure 2.2.2 - Pharmacological-mediated perturbation of the LCMT1-PME-1 methylation equilibrium leads to small spindle size. (**A**) Quantification of metaphase spindle PTP distance (in µm) showing that AMZ30-treated cells have abnormally short spindles. (**B**) Quantification of metaphase spindle width (in µm) showing that AMZ30-treated cells have abnormally short spindle widths. (**C**) Quantification of metaphase spindle volume (in μm^3) showing that treatment with AMZ30 leads to a decrease in volume. (**D**) Quantification of the total fluorescence intensity of mitotic spindle microtubules for AMZ30-treated cells, in arbitrary units (A.U.), showing that AMZ30 treatment leads to a decrease in total microtubules. (**A-D**) Data represents average ± SDs of three independent experiments. **=P<0.005, ***=P<0.0005.

2.3 Perturbation of the LCMT1-PME-1 methylation equilibrium by overexpressing LCMT1 or PME-1 leads to an abnormal mitotic spindle size

To further test this hypothesis, we generated doxycycline (Dox) inducible localization and affinity purification (LAP) tagged LCMT1 and PME-1 HeLa stable cell lines that expressed either LAP-LCMT1 or LAP-PME-1 from a single locus within the genome.[12] These cell lines were used to analyze the effects of overexpressing LAP-LCMT1 or LAP-PME-1 on spindle size and morphology. Briefly, cells were treated with Dox for 24 hours to induce LAP-LCMT1 or LAP-PME-1 overexpression. Cells were then harvested and protein extracts were analyzed by immunoblot analysis (**Fig. 2.3.1**).

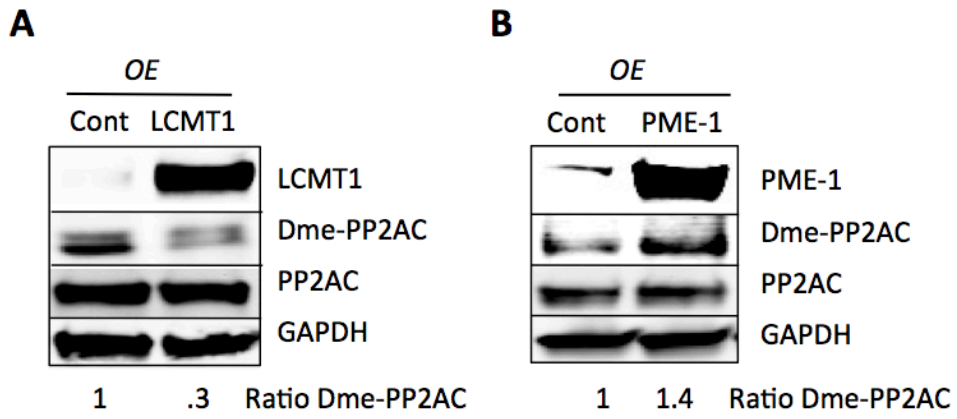

Figure 2.3.1 – Overexpression of LCMT1 and PME-1. (**A-B**) Overexpression of LAP-LCMT1 (**A**) or LAP-PME-1 (**B**) compared to non-induced control cells. Note that the levels of demethylated PP2AC decreased in cells overexpressing LAP-LCMT1 and increased in cells overexpressing LAP-PME-1.

In parallel experiments, cells overexpressing LAP-LCMT1 or LAP-PME-1 were fixed, stained, and their mitotic defects, spindle size, and spindle volume were analyzed by immunofluorescence microscopy as described above. These analyses showed that overexpression of LAP-PME-1 led to longer spindles with spindle multipolarity and unaligned chromosomes (**Fig. 2.3.2A-B**). Conversely, overexpression of LAP-LCMT1 led to shorter spindles with chromosomes not fully aligned at the metaphase plate (**Fig. 2.3.2A-B**). Quantitative analysis of these data showed that overexpression of LAP-LCMT1 or LAP-PME-1 led to a major increase in

the percentage of cells arrested in mitosis (LAP-LCMT1= 34.3±7.9 (p=0.01) and LAP-PME-1= 36.0±2.4 (p=0.0002) compared to Control= 10.0±1.6) (**Fig. 2.3.2C**), an increase in the percentage of cells with abnormal mitotic spindles (short, long, multipolar) (predominantly short spindles for LAP-LCMT= 39.3±4.2 (p=0.0028) compared to Control= 4.7±1.2 and long spindles= 28.0±4.9 (p=0.0026) and multipolar spindles= 29.7±3.4 (p=0.0086) for LAP-PME-1 compared to Control= 6.0±1.6 and 9.3±1.2 respectively) (**Fig. 2.3.2D**), and an increase in the percentage of cells with unaligned chromosomes (LAP-LCMT1= 28.3±4.5 (p=0.0052) and LAP-PME-1= 46.7±2.9 (p=0.0002) compared to Control= 12±1.4) (**Fig. 2.3.2E**).

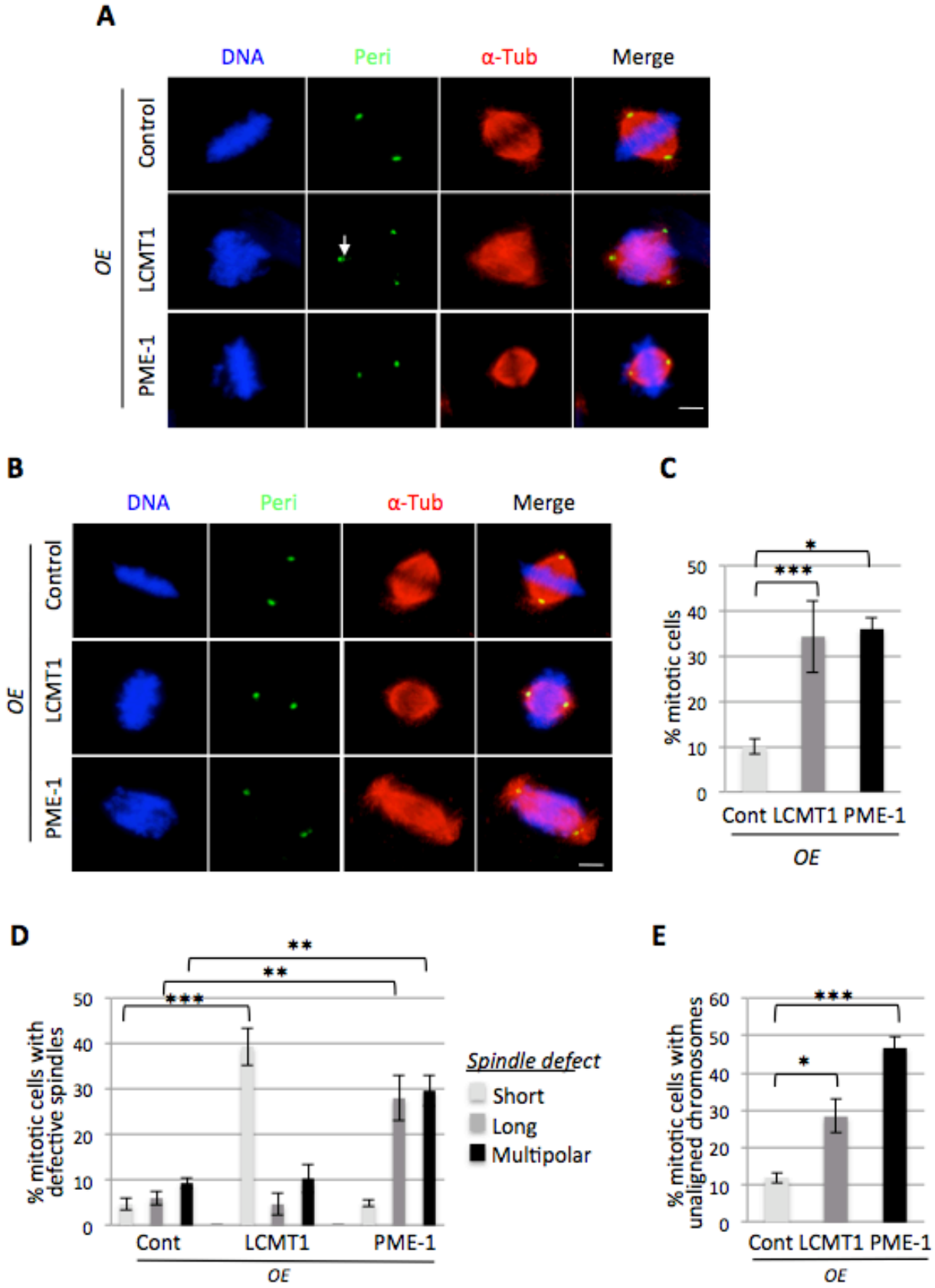
A
DNA
Peri
α-Tub
Merge
Control
LCMT1
PME-1
OE
B
DNA
Peri
α-Tub
Merge
Control
LCMT1
PME-1
OE
C
% mitotic cells
50
40
30
20
10
0
*
***
Cont
LCMT1
PME-1
OE
D
% mitotic cells with defective spindles
50
40
30
20
10
0
**
**
***
Cont
LCMT1
PME-1
OE
Spindle defect
Short
Long
Multipolar
E
% mitotic cells with unaligned chromosomes
60
50
40
30
20
10
0
***
*
Cont
LCMT1
PME-1
OE

Figure 2.3.2 - Perturbation of the LCMT1-PME-1 methylation equilibrium by overexpression leads to spindle assembly defects. (**A**) Immunofluorescence microscopy of cells with indicated treatments stained for DNA (Hoechst 33342), α-tubulin (anti-α-tubulin antibodies) and Pericentrin (anti-pericentrin antibodies). Overexpression of LCMT1 leads to short spindles with unaligned chromosomes (see white arrows), while PME-1 overexpression lead to long multipolar or fragmented spindles with unaligned chromosomes. Bar=5μm. (**B**) Immunofluorescence microcopy showing that LAP-PME-1 overexpression leads to abnormally long spindles and LAP-LCMT1 overexpression leads to abnormally short spindles. Bar= 5μm. (**C**) Quantification of the percentage of cells in mitosis showing that overexpression of LAP-PME-1 or LAP-LCMT1 leads to a major increase in cells arrested in mitosis. (**D**) Quantification showing that overexpression of LAP-LCMT1 or LAP-PME-1 leads to a major increase in the percentage of abnormal spindles (short, long, multipolar). (**E**) Quantification showing that overexpression of LAP-LCMT1 or LAP-PME-1 leads to a major increase in the percentage of unaligned chromosomes. (**C-E**) Data represents average ± SDs of three independent experiments. *=P< 0.05, **=P<0.005, ***=P<0.0005, ns= not statistically significant.

Consistent with our previous results, control cells had a PTP distance of 10.8μm±.41, whereas in cells overexpressing LAP-PME-1 metaphase spindles were longer (PTP distance= 12.8μm±.31, p=0.02) and those overexpressing LAP-LCMT1 displayed shorter spindles (PTP distance= 7.3μm±.3, p=0.0065) (**Fig. 2.3.3A**). However, LAP-PME-1 cells had a similar spindle width (8.9μm±.1) to siControl cells (8.8μm±.25), whereas the spindle width of LAP-LCMT1 cells was shorter (6.8μm±.26, p=0.0057) (**Fig. 2.3.3B**). Interestingly, the spindle volume was abnormally large for cells overexpressing LAP-PME-1 (527μm±20.5, p=0.0066) and abnormally small for cells overexpressing LAP-LCMT1 (181μm±21.5, p=0.0012), compared to control spindles (434.3μm±14.4) (**Fig. 2.3.3C**). There was also a reduction in the total fluorescence intensity of spindle microtubules for cells overexpressing LAP-LCMT1 (317 A.U.±31, p=0.05) and LAP-PME-1 (587 A.U.±39, p=0.03) compared to control (438±53 A.U.) (**Fig. 2.3.3D**). In addition, overexpression of LAP-LCMT1 led to a decrease in the ratio of demethylated PP2AC (Control=1±.06, LAP-LCMT1=0.3±.02), whereas LAP-PME-1 overexpression led to an increase

in the ratio of demethylated PP2AC (Control=1±.01, LAP-PME-1=1.4±.06) (**Fig. 2.3.1**). These results were consistent with the proposed model where a LCMT1-PME-1 methylation equilibrium was responsible for regulating spindle size through the modulation of PP2AC methylation (**Fig. 2.1.3F**).

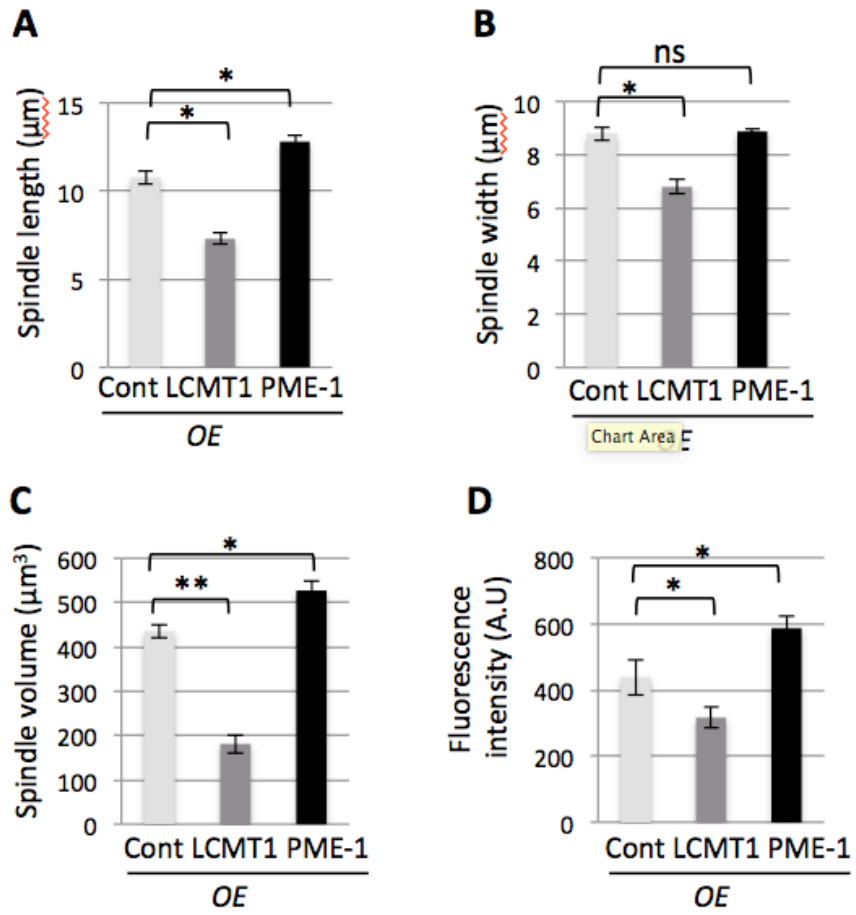

Figure 2.3.3 - Perturbation of the LCMT1-PME-1 methylation equilibrium by overexpression leads to abnormal mitotic spindle size. (**A**) Quantification of metaphase spindle PTP distance (in µm) showing that LAP-PME-1 overexpression leads to abnormally long spindles and LAP-LCMT1 overexpression leads to abnormally short spindles. (**B**) Quantification of metaphase spindle width (in µm) showing that overexpression of LAP-LCMT1 leads to a decrease in spindle width, while overexpression of LAP-PME-1 had no significant effect on spindle width. (**C**) Quantification of metaphase spindle volume (in μm^3) showing that overexpression of LAP-PME-1 leads to an increase in volume and LAP-LCMT1 overexpression leads to a decrease in volume. (**D**) Quantification of the total fluorescence intensity of mitotic spindle microtubules for LAP-PME-1 or LAP-LCMT1 overexpressing cells, in arbitrary units

(A.U.), showing that overexpression of LAP-PME-1 or LAP-LCMT1 leads to a decrease in total microtubules. (**A-D**) Data represents average ± SDs of three independent experiments. *=P< 0.05, **=P<0.005, ***=P<0.0005, ns= not statistically significant.

2.4 Perturbation of the LCMT1-PME-1 methylation equilibrium leads spindle assembly checkpoint activation, an induction of apoptosis and reduced cell viability

Since perturbation of the LCMT1-PME-1-methyaltion equilibrium led to an increase in unaligned chromosomes at the meta- phase plate, we sought to understand whether these defects were due to defects in kinetochore-microtubule attachment. First, we measured the total amount of cold-stable microtubule polymer (total fluorescence intensity of cold-stable microtubules, which form proper kinetochore-microtubule attachments in arbitrary units (A.U.)) in LCMT1 or PME-1 depleted cells, PME-1 inhibited cells and LAP-LCMT1 or LAP-PME-1 overexpressing cells. While there was a statistically significant decrease in the fluorescence intensity of cold-stable microtubules in PME-1 depleted cells, PME-1 inhibited cells and LCMT1 overexpressing cells, there was only a small decrease in LCMT1-depleted and PME-1 overexpressing cells that was not statistically significant (**Fig. 2.4.1A–C**). However, the lack of a significant difference in LCMT1-depleted and PME-1 overexpressing cells could have been due to the fact that these cells had elongated spindles and thus more tubulin polymer to start with. Thus, we turned to an alternative assay to analyze kinetochore-microtubule attachment. Here, we asked if perturbation of the LCMT1-PME-1-methyaltion equilibrium could activate the spindle assembly checkpoint (SAC), which responds to unattached kinetochores or non-productive microtubule-kinetochore attachments, by monitoring the localization of the SAC kinase Bub1 (localizes to the kinetochore when the SAC is active). Indeed, depletion of LCMT1 or PME-1, inhibition of PME-1 and overexpression of LAP-LCMT1 or LAP-PME-1 led to SAC activation even in cells that appeared to have all their chromosomes aligned at the metaphase plate (**Fig. 2.4.1D–F**) Together

these data indicated that perturbation of the LCMT1-PME-1-methyaltion equilibrium leads to defects in microtubule-kinetochore attachment and activation of the SAC.

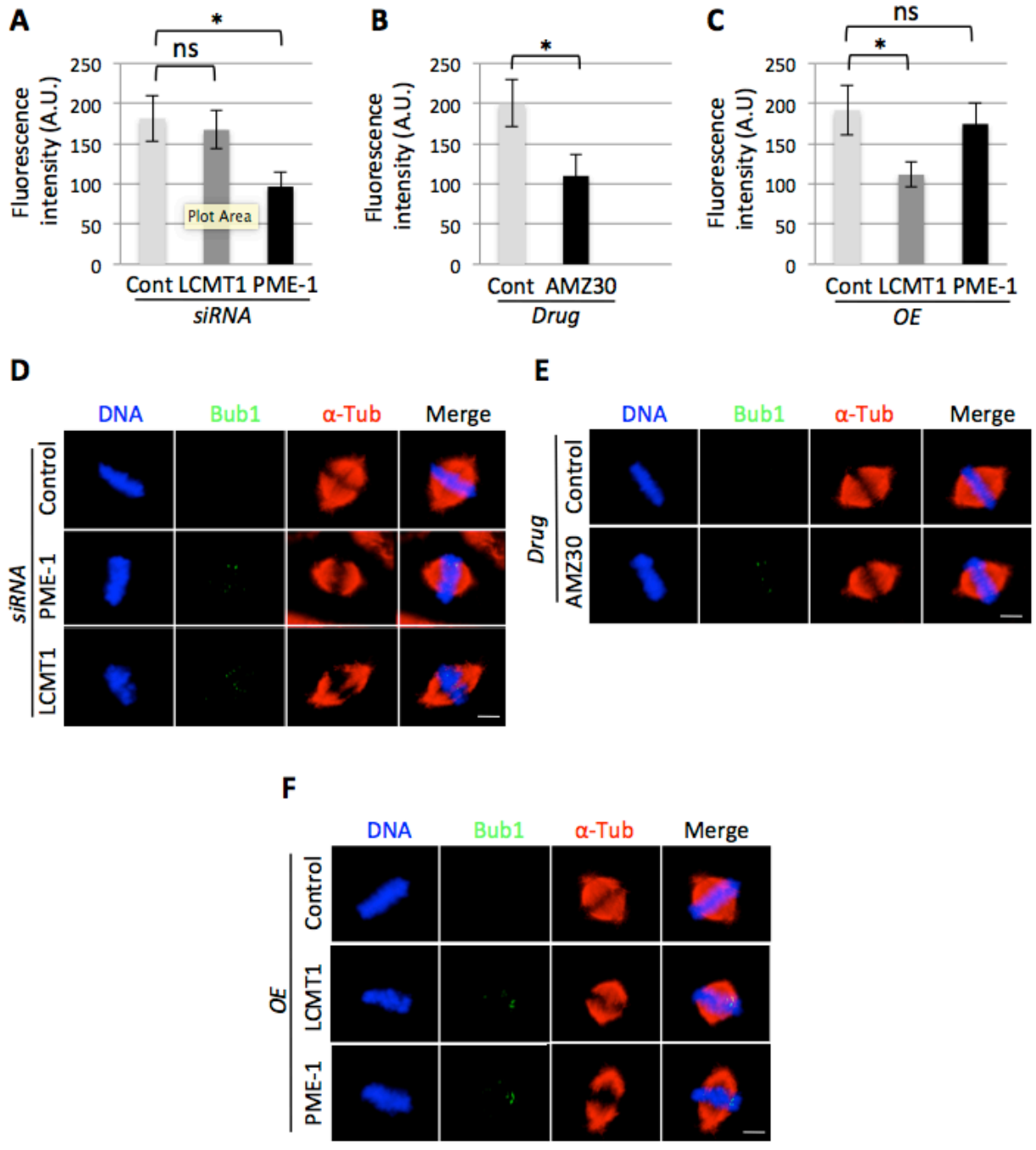

Fig 2.4.1 - Perturbation of the LCMT1-PME-1 methylation equilibrium leads to defects in microtubule-kinetochore attachment and activation of the SAC. (**A-C**) Quantification of the

total fluorescence intensity of cold treated mitotic spindle microtubules for PME-1 or LCMT1-depleted (**A**), AMZ30-treated cells (**B**), or PME-1 or LCMT1-overexpressing cells (**C**). A.U. indicates arbitrary units. Data represents average ± SDs of three independent experiments. (**D-F**) Fixed-cell immunofluorescence microcopy showing that the spindle assembly checkpoint is activated (Bub1 remains localized to kinetochores) in LCMT1 or PME-1 depleted cells (**D**), PME-1 inhibited cells (**E**) and LCMT1 or PME-1 overexpressing cells (**F**). Bar= 5μm. (**A-C**) Data represents average ± SDs of three independent experiments. *=P< 0.05, **=P<0.005, ***=P<0.0005, ns= not statistically significant.

Next, we asked if the misregulation spindle size had an effect on cell viability by measuring the effect of these treatments on cell viability using the CellTiter-Glo luminescent cell viability assay, which measured total ATP levels indicative of metabolically active cells. This analysis revealed that cell viability decreased in cells with a perturbed methylation equilibrium (normalized percent cell viability for siLCMT1= 66±1.45, p<.005; siPME-1= 66±2.24, p<.005; PME-1 inhibition= 62±3.2, p<.05); LCMT1 overexpression= 80±2.7, p<.005; PME-1 overexpression= 82±1.8, p<.005) (**Fig. 2.4.2A–C**). Additionally, we analyzed whether this decrease in cell viability was due to the activation of the apoptotic cell death pathway by immunoblotting cell lysates for cleaved Caspase 3. Indeed, perturbation of the methylation equilibrium (through inhibition/depletion or overexpression of LCMT1 or PME-1) led to an increase in Caspase 3 cleavage, indicative of apoptosis (**Fig. 2.4.2D–F**). Together these data indicated that perturbation of the LCMT1-PME-1-methylation equilibrium led to a caspase-mediated cell death.

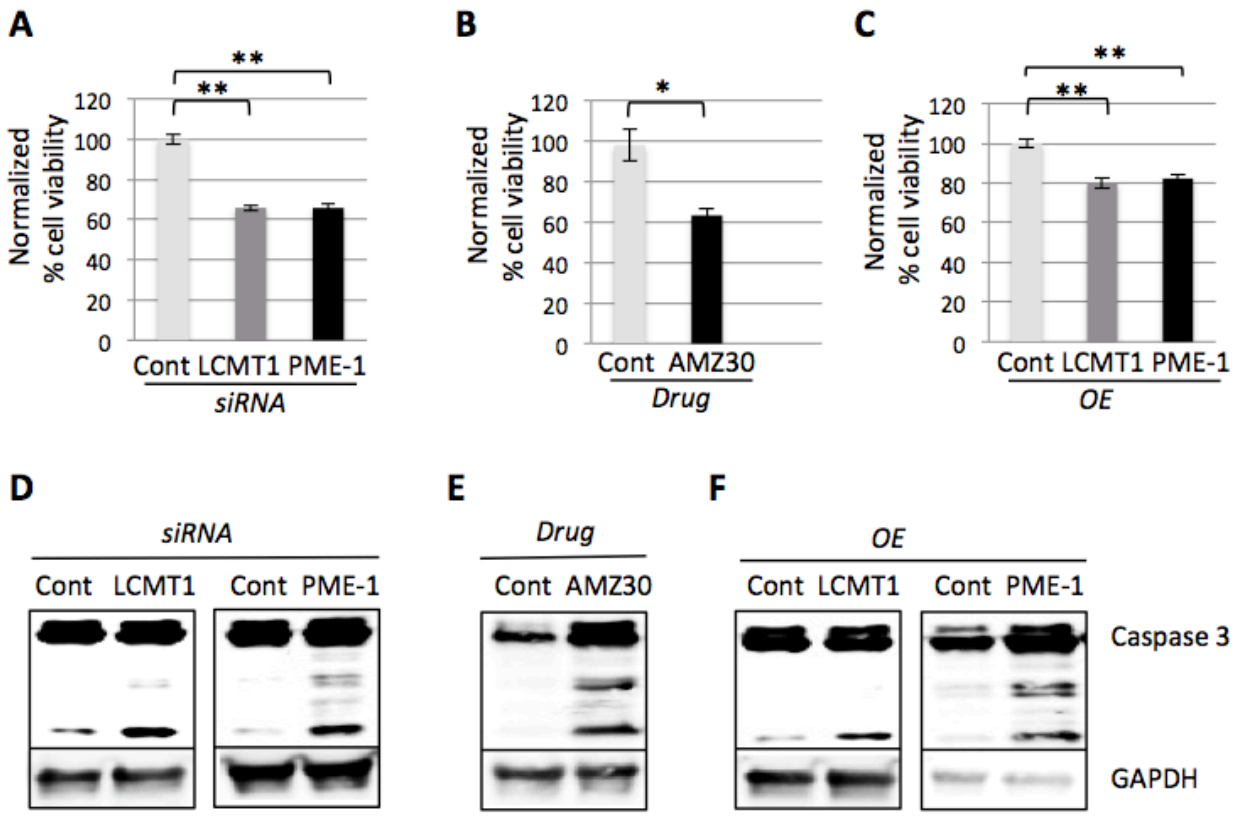

Fig 2.4.2 - Perturbation of the LCMT1-PME-1 methylation equilibrium leads to caspase-mediated cell apoptosis. (**A-C**) Quantification of normalized percent cell viability for LCMT1 or PME-1-depleted (**A**), AMZ30-treated (**B**), or LCMT1 or PME-1-overexpressingcells (**C**). (**D-E**) Perturbation of the LCMT1-PME-1 methylation equilibrium induces apoptosis. Immunoblot analysis of Caspase 3 cleavage for LCMT1 or PME-1-depleted (**D**) , AMZ30-treated (**E**) , or LCMT1 or PME-1-overexpressing cells (**F**). (**A-C**) Data represents average ± SDs of three independent experiments. *=P< 0.05, **=P<0.005.

Finally we analyzed the consequences of perturbing the LCMT1-PME-1 methylation equilibrium by live-cell time-lapse microcopy. siControl, siLCMT1, siPME-1, control DMSO, AMZ30, uninduced and LAP-LCMT1 or LAP-PME-1 overexpressing HeLa cells were synchronized in G1/S (thymidine treatment) and released into the cell cycle. Six hours post-release, cells were imaged at 20X magnification every 15-minutes and images were processed into movie format (**Fig. 2.4.3A-C**). The movies were then analyzed to determine the percentage of cells that arrested in mitosis (MA), that displayed defective divisions (DD) or that died during

mitosis (DM) (**Fig. 2.4.3D-F**). Consistent with previous data, perturbation of the methylation equilibrium led to an increase in the percentage of cells that arrested during mitosis, that had defective divisions and that died during mitosis (**Fig. 2.4.3D-F**). Additionally, we quantified the time spent in mitosis (time length from cell rounding to cell abscission) for each treatment (**Fig. 2.4.3G-I**). Whereas control cells transitioned through mitosis within 90 minutes, perturbation of the LCMT1-PME-1 methylation equilibrium led to an increase in the time (hours) cells spent in mitosis (siLCMT1 =1.61±.53 (p=0.0001) and siPME-1 =3.36±1.5 (p=0.0001) compared to siControl= 8.7±1.7 (**Fig. 2.4.3G**); AMZ30= 6.37±2.3 (p=0.0001) compared to DMSO= 1.36±.42 (**Fig. 2.4.3H**); LAP-LCMT1= 5.46.±1.59 (p=0.002) and LAP-PME-1= 4.30±1.3 (p=0.001) compared to control= 1.86±.48) (**Fig. 2.4.3I**). These data were consistent with fixed-cell immunofluorescence microscopy data and further indicated that changes in spindle length can lead to increased mitotic arrest and increased cell death.

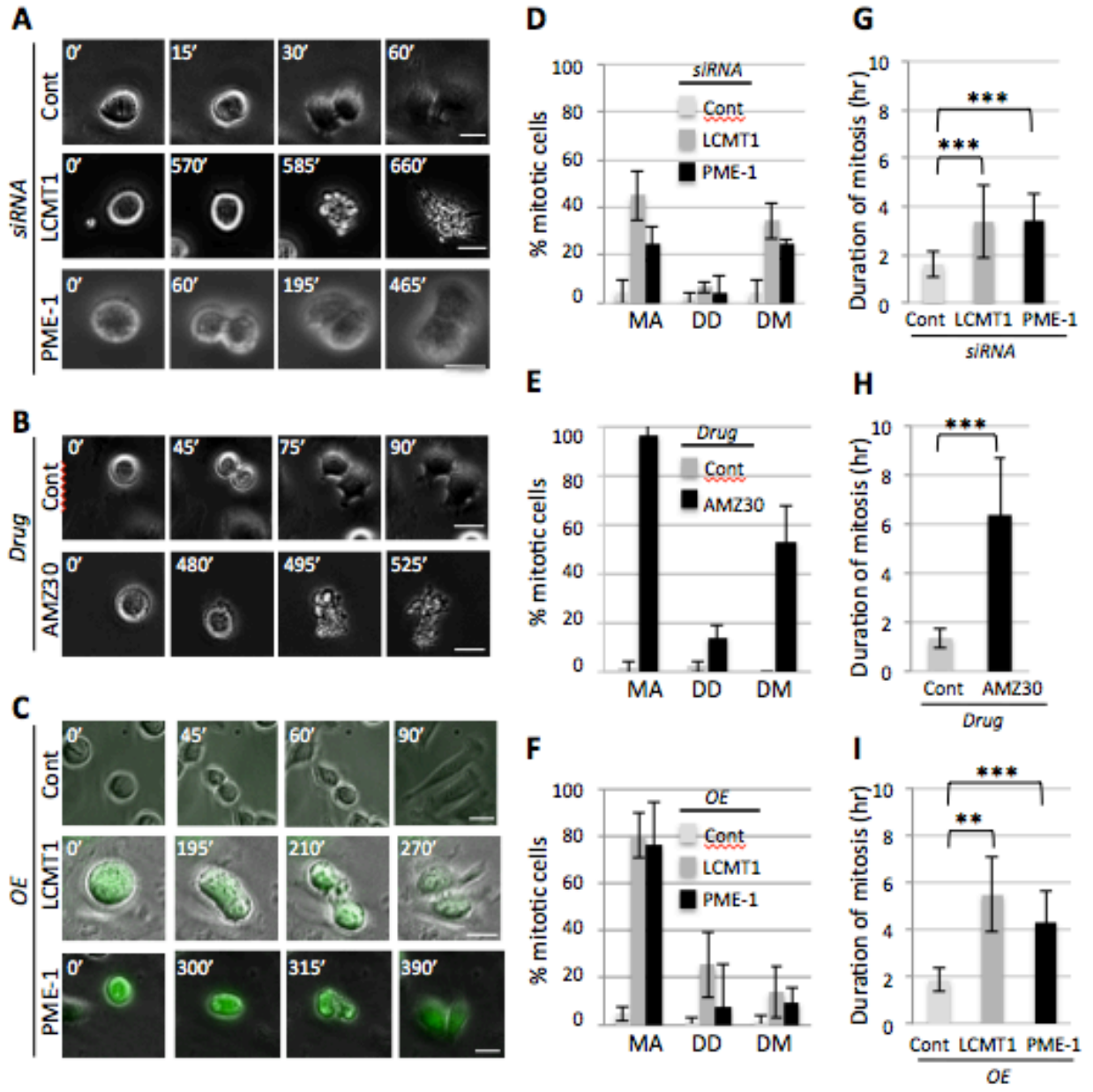

Figure 2.4.3. Analyzing the consequences of perturbing the LCMT1-PME-1 equilibrium by live-cell time-lapse microscopy. (**A**) Live-cell imaging of siControl, siLCMT1 or siPME-1 treated cells. (**B**) Live-cell imaging of control DMSO or AMZ30 treated cells. (**C**) Live-cell imaging of LAP-LCMT1 or LAP-PME-1. (**A-C**) Bar= 20µm. Time is in minutes. (**D-F**) Quantification of the live-cell imaging data from A-C for the percentage of cells undergoing mitotic arrest (MA), defective cell divisions (DD) and cell death in mitosis (DM). Data represents average ± SDs of four independent experiments. (**G-I**) Quantification of live-cell imaging data from A-C for the length of time cells spent in mitosis. Data represents average ± SDs of four independent experiments. **=P< 0.005, ***=P<0.0005.

CHAPTER 3 – DISCUSSION

Together, these data indicate that LCMT1 and PME-1 are novel factors important for regulating spindle size and cell division. We propose that a balance between LCMT1 methylation and PME-1 demethylation is critical for controlling spindle size through the methylation of PP2AC and that misregulating this equilibrium leads to defective spindle assembly and decreased cell viability due to activation of the apoptotic pathway (**Fig. 2.1.3F**). This study increases our understanding of the enzymatic machinery (LCMT1 and PME-1) that regulates mitotic spindle size and implicates methylation as an important regulatory posttranslational modification for establishing proper spindle size.

PP2A holoenzyme complexes have varied roles during mitotic entry, mitotic spindle assembly and mitotic exit.[13-16] Although much of the characterization of PP2A complexes has been carried out in model organisms like yeast and flies, humans have a larger number (~15) of regulatory B-subunits (B, B', B'', B'''), which further complicates the analysis of the function of PP2A and studies analyzing the effect of depleting specific B-subunits in mitosis have been most insightful.[2] Previously, we systematically depleted each B-subunit from human cells and analyzed their defects in early mitosis, among the B-subunits with defects in mitosis was the B type subunit PPP2R2B (R2B).[13] B type subunits (PPP2R2A, PPP2R2B, PPP2R2C, PPP2R2D) require PP2AC methylation by LCMT1 to bind to PP2AC and form active holoenzymes, whereas other B-subunits do not necessitate this posttranslational modification to form active holoenzymes.[2, 4] Interestingly, the PP2AC/R1A/R2B holoenzyme was required for de-phosphorylating the Anaphase Promoting Complex/Cyclosome (APC/C) subunit Cdc27 to allow its association with mitotic spindle microtubules to regulate proper mitotic spindle formation.[13] Additionally, cells depleted of R2B also displayed elongated spindles and spindle

multipolarity. Therefore it was possible that the LCMT1-PME-1 methylation equilibrium was indirectly controlling the phosphorylation state of the APC/C, and thereby mitotic spindle assembly, through PP2AC/R1A/R2B.[13] Consistent with this idea, wildtype cells arrested in mitosis with nocodazole maintained Cdc27 in its expected hyper-phosphorylated form, whereas in AMZ30 treated cells Cdc27 was dephosphorylated (hypo-phosphorylated) (**Fig. 3.1.1**). Although preliminary, these results indicate that the LCMT1-PME-1 methylation equilibrium could potentially act through regulating the assembly of the PP2AC/R1A/R2B complex and thereby the phosphorylation/dephosphorylation of the APC/C to control spindle size and should be explored further.

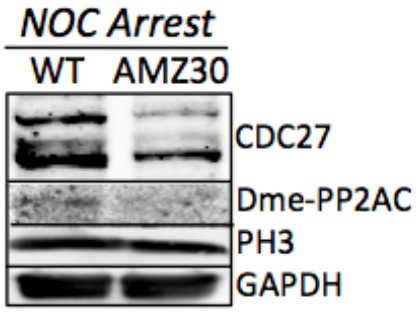

Figure 3.1.1- Inhibition of PME-1 leads to a decrease in APC/C phosphorylation in mitotic (nocodazole arrested) cells. Immunoblot analysis of AMZ30-treated (PME-1-inhibited) cells. Note that AMZ30 treatment leads to a decrease in demethylated PP2AC and a decrease in Cdc27 phosphorylation in mitosis.

However, there are several other interpretations as to how PP2A may be regulating spindle size. For example, the B type subunit PPP2R2A (which is dependent on LCMT1 PP2AC methylation in order to assemble into the PP2AC/R1A/R2A holoenzyme) has been implicated in regulating the phosphorylation state of the microtubule-associated protein Tau, which may affect the stability of microtubules and thereby length.[17, 18] Although B' subunits have been implicated in the regulation of centromere cohesion and the formation of stable kinetochore-microtubule attachments that could lead to differences in spindle size, this is unlikely as B' subunits are not dependent on PP2AC methylation for holoenzyme assembly.[4, 19, 20] Finally,

molecular motors (like Kinesin-5), microtubule polymerization proteins (like XMAP215), microtubule depolymerization proteins (like Kinesin-8), and microtubule severing enzymes (like Katanin) have been shown to influence mitotic spindle size and the signaling pathways, posttranslational modifications and protein-protein interactions that regulate these factors remain poorly characterized.[21-25] Thus, although PP2AC is the only known direct substrate that is modified by the LCMT1-PME-1 methylation equilibrium, it is still possible that Kinesin-5, Kinesin-8, XMAP215, Katanin or other proteins that influence microtubule spindle length could be direct targets of LCMT1/PME-1 and should be evaluated.

CHAPTER 4 – MATERIAL AND METHODS

4.1 Cell culture

HeLa cell culture and synchronizations were as described previously.[26] For pharmacological inhibition of PME-1, cells were treated with 10μM AMZ30 for the indicated times.

4.2 RNAi

For RNA interference experiments, the following Dharmacon ONTARGETplus siRNAs: siControl (cat# D-001810-10), siLCMT1 (pool and individual oligos, cat# L-009425-00, -06, -07, -08, -09) or siPME-1 (pool and individual oligos, cat# L-005211-00, -05, -06, -07, -08) were used at 50nM to transfect HeLa cells using Lipofectamine RNAiMAX as described by the manufacturer (Invitrogen).

4.3 Cloning and generation of LAP-tagged stable cell lines

For full-length LCMT1 and PME-1 expression, full-length LCMT1 or PME-1 cDNA was fused to the c-terminus of EGFP (pGLAP1 vector) and vectors were used to generate doxycycline inducible HeLa Flp-In-T-REx LAP-LCMT1 or PME-1 stable cell lines that express these proteins from a single locus within the genome as described previously.[12]

4.4 Antibodies

Immunofluorescence and immunoblotting were carried out using antibodies that recognize: GFP (Invitrogen cat#A-11120), Gapdh (Covance cat#MMS-580S), α-tubulin (Serotec cat#MCAP77), LCMT1 and PME-1 (Santa Cruz Biotechnology cat#SC-134675 and cat#SC-25278), PP2AC

(Cell Signaling Technology cat#2038S), de-methylated PP2AC (EMD Millipore cat#05-577), Caspase 3 (Cell Signaling Technology cat#9665), Pericentrin (Novus Biologicals cat#NB100-61071), Bub1 (kind gift from Hongtao Yu). Secondary antibodies conjugated to FITC, Cy3, and Cy5 were from Jackson Immuno Research (Affinipure).

4.5 Fixed-cell and live-cell microscopy

Fixed-cell immunofluorescence microscopy was carried out as described previously.[13]

Except that images were captured with a Leica DMI6000 microscope (Leica DFC360 FX Camera, 63x/1.40-0.60 NA oil objective, Leica AF6000 software). Images were deconvolved with Leica Application Suite 3D Deconvolution software and exported as TIFF files. Live-cell time-lapse microscopy was carried out as described previously.[27] Except that *Z*-stacks were captured every 1 μm for 10 μm at 20X magnification, and stacks were deconvolved with Leica Application Suite 3D Deconvolution software and compressed as maximum intensity projection images. Images were then converted to movies using QuickTime software (Apple). Each frame represents a 15-minute interval.

4.6 Cell viability and Caspase 3 cleavage assays

The cell viability of cells treated with indicated siRNAs for 72 hours, drugs for 24 hours or induced to over express LCMT1 or PME-1 for 48 hours was determined using the CellTiter-Glo Assay (Promega) as described previously.[28] To monitor Caspase 3 cleavage, cells were subjected to the above-mentioned treatments and protein extracts from these cells were analyzed by immunoblot analysis with anti-Caspase 3 antibodies.

4.7 Quantification of data and statistical analysis

For percent abnormal spindles, spindle defects (long, short, multipolar) were quantified for each treatment (using 100 spindles for each treatment in each of three independent experiments). For spindle size pole-to-pole measurements, a vector was drawn connecting the two pericentrin stained poles and the vector distance (μm) was quantified for each treatment (using 20 spindles for each treatment in each of three independent experiments). Spindle volume ($V=\alpha LA_o$) measurements in μm^3 were quantified as described previously[22], with 20 spindles for each treatment in each of three independent experiments. Spindle PTP distance and volume were measured using Leica AF6000 software. The total fluorescence intensity of spindle microtubules and cold-treated spindle microtubules was measured 10 spindles for each treatment in each of three independent experiments using Leica AF6000 software. For all measurements, data represent the average ± SD of three independent experiments. Statistical differences were calculated using a student's t-test. $P< 0.05$ was considered statistically significant.

Pharmacological Inhibition of the Leukemia Cell Cycle Identifies Specific Inhibitors of Leukemia Cell Proliferation

CHAPTER 4 – INTRODUCTION

Acute lymphoblastic leukemia (ALL) originates from single B- or T-lymphocyte progenitors that proliferate and accumulate, resulting in the suppression of normal hematopoiesis [29]. Each year, there are about 6,000 newly diagnosed cases of ALL in the USA, affecting both children and adults. The treatment of ALL has been one of the greatest successes in cancer therapy [30]. Decades of anti-leukemia research and development have yielded multi-agent chemotherapy regimens, CNS prophylaxis and extended maintenance regimens. These therapeutic advancements together with risk-adapted treatment strategies have significantly improved treatment outcomes in ALL patients. In pediatric ALL, overall cure rates are approaching 90%, but there are still subgroups remaining that are unresponsive to the current treatments. Relapse ALL is still a leading cause of cancer-related deaths in the pediatric population, and in adult ALL, long-term survival rates are only between 35% to 50% [31]. This is partly due to leukemia cell drug resistance mechanisms and the limited efficacy, lack of specificity and toxic side effects of current drugs used to treat leukemia [32-35]. Therefore, continuous efforts to identify novel molecular targets and development of novel drug-like molecules are in critical needs.

Currently, there are many types of chemotherapeutics for ALL available, including glucocorticoids, microtubule inhibitors, anthracyclines, purine and folate antimetabolites, asparaginases and DNA alkylating agents. Among these, one successful strategy has been to inhibit leukemia cell proliferation by targeting DNA synthesis, protein synthesis, cell cycle progression, and proliferation-promoting signaling cascades [29]. For example, Methotrexate which has been used in ALL treatment since 1953, blocks cells in S phase of the cell cycle by inhibiting *de novo* purine synthesis and folate metabolism [36]. Another widely used drug in ALL chemotherapy, Vincristine, affects mitotic spindle formation by binding to tubulin,

ultimately arrests cells in mitosis and leads to cell apoptosis [37]. However, due to drug resistance and toxicity issues associated with these drugs [38], numerous effects has been put into improving the therapeutic index of standard antileukemic agents [39, 40]. One approach has been used extensively is to come up with new formulation of old drugs, like encapsulating drugs into liposomes to increase specificity and circulation time in the bloodstream [41-44]. Despite continuous R&D over the past decades, with the exception of tyrosine kinase inhibitors for Ph^+ ALL, there has been no new FDA approvals of ALL treatment since 2006 [31].

Most leukemia drug discovery studies have relied on predefined targets identified by genetic abnormalities, differential gene expression or protein abundance between normal and disease states [45, 46]. Traditional target-based drug discovery is then used to identify inhibitors to these targets [47]. However, this process often relies on *in vitro* activity assays and candidate inhibitors are frequently not cell permeable, lose their activity or have unintended consequences within the context of the cell, primarily due to off-target effects [48]. As an alternative approach, chemical genetic drug discovery approaches have utilized cell based assays to identify anticancer agents, which has been highly successful with adherent cancer cells [48]. However, the difficulty in utilizing suspension cells for high-throughput chemical screens has hampered the progress in identifying novel inhibitors of blood born cancers. Therefore, only a limited number of compounds have been tested for their anticancer activities on human acute myeloid leukemia or lymphoma cells [49, 50]. These screens have relied on fluorescence activated cell sorting (FACS) instruments that are not amenable to high-throughput screening, or on endpoint viability assays that lack critical information with regards to the phase of the cell cycle where these compounds are active [49, 50]. In addition, a major bottleneck of chemical genetic screens is the difficulty in identifying the targets of bioactive compounds, a critical step in understanding the

mechanism of action for these inhibitors and their potential for chemical modification to improve their therapeutic potential [51]. Here, we report the development and use of a novel leukemia suspension cell-based high-throughput chemical screening approach that relies on leukemia cell cycle profiling. This approach identified novel G1/S, G2 and M-phase specific leukemia inhibitors with diverse chemotypes. Most importantly, we have identified and characterized a leukemia specific inhibitor (Leusin-1), which specifically arrests leukemia cells during G2-phase and triggers an apoptotic cell death. G2 arresting compound, like Daunorubicin, remains as a standard for treating ALL for the past forty years [52]. Nevertheless, there is a critical need to identify novel synthetic molecules that can address the limitations of Daunorubicin, which includes but not limited to, cardiotoxicity and multidrug resistance [53, 54]. Thus, Leusin-1 represents an opportunity to develop improved alternatives.

CHAPTER 5 – RESULTS

5.1 Discovery of Leukemia cell cycle modulators

The limited efficacy, lack of specificity and toxic side effects of current antileukemic drugs [32-35], inspired us to establish an integrated high-throughput suspension cell-based strategy to identify small molecule cell cycle modulators for use in dissecting the mechanisms of leukemia cell proliferation and for the development of novel leukemia therapies (**Fig 5.1.1A**). Briefly, human CCRF-CEM ALL cells are plated into 384 well plates. A diverse compound library (181,420 small drug-like molecules) encompassing broad chemical space was used to place one compound per well at a final concentration of 10 μM. Sixteen hours later the cells were fixed and stained with the DNA-selective stain Vybrant DyeCycle Green, which emits a fluorescent signal that is proportional to a cells DNA mass when exited at 488 nm. Plates were then scanned with an Acumen ^{e}X3 fluorescence microplate cytometer using its 488 nm laser and a cell cycle histogram profile was generated for each compound (**Fig 5.1.1A**). Cell cycle profiles were ranked according to percent G1/S-phase arrest and percent G2/M-phase arrest (**Fig 5.1.1B-C** and **Table S2**). An example of a compound from each class and its associated cell cycle profile are shown (**Fig 5.1.1D-E**). Compounds that arrested cells in G1/S-phase with >4 STDs from the DMSO control or in G2/M-phase with >80% of the Taxol control were retested in triplicate to confirm their bioactivity. In total 30 G1/S-phase and 483 G2/M-phase inhibitors were reconfirmed and they accounted for an overall hit rate of .29% (**Fig 5.1.1F** and **Table S1**).

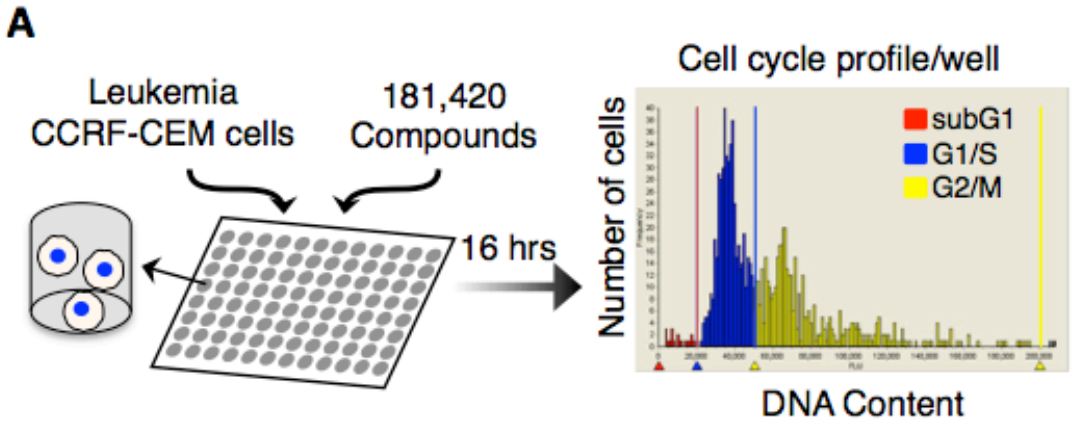
A
Leukemia
CCRF-CEM cells
181,420
Compounds
16 hrs
Cell cycle profile/well
Number of cells
subG1
G1/S
G2/M
DNA Content

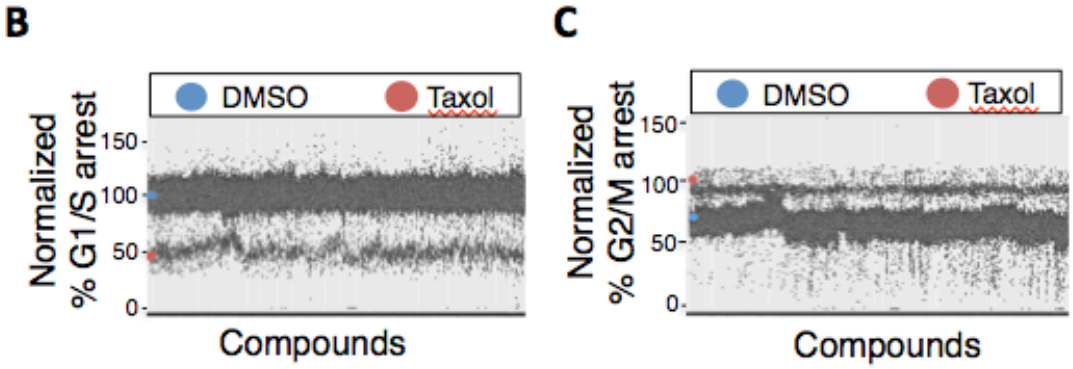
B
DMSO
Taxol
Normalized
% G1/S arrest
150
100
50
0
Compounds
C
DMSO
Taxol
Normalized
% G2/M arrest
150
100
50
0
Compounds

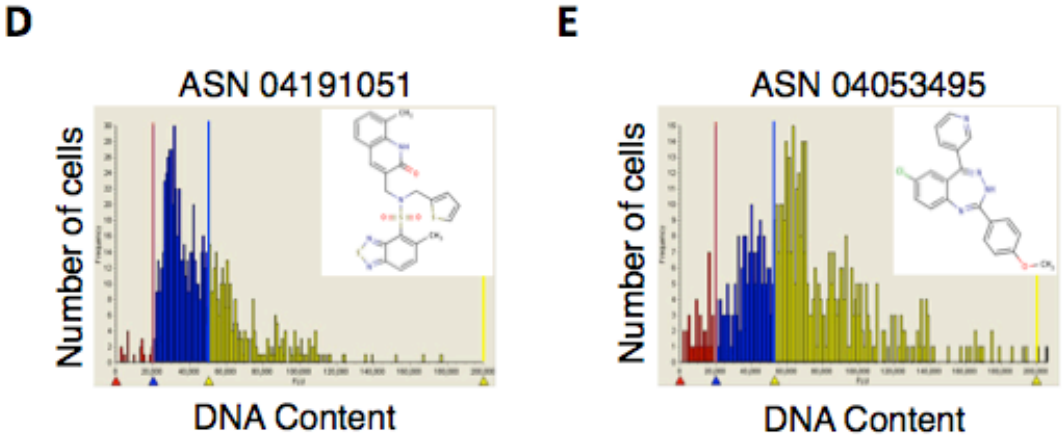
D
ASN 04191051
Number of cells
DNA Content
E
ASN 04053495
Number of cells
DNA Content

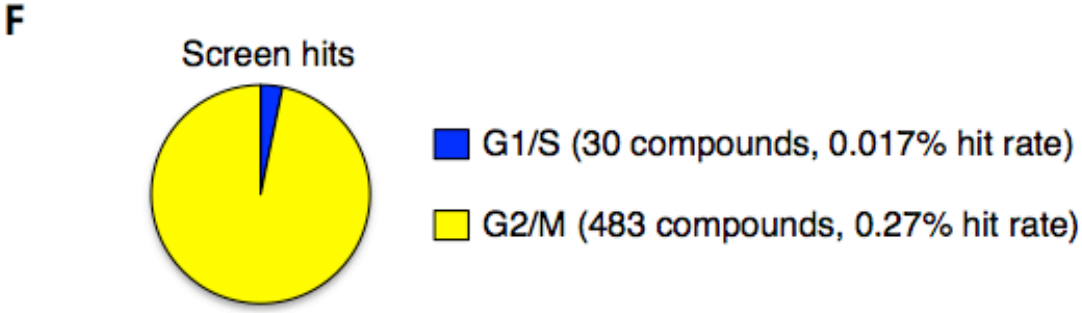
F
Screen hits
G1/S (30 compounds, 0.017% hit rate)
G2/M (483 compounds, 0.27% hit rate)

Figure 5.1.1 - Overview of the leukemia suspension cell-based high-throughput chemical screening approach and summary of screen results. (**A**) Leukemia CCRF-CEM cells were treated with each of 181,420 compounds for sixteen hours. Cells were then fixed and stained with Vybrant DyeCycle green and a cytometer was used to generate a cell cycle profile for each compound based on the fluorescence intensity that is proportional to a cells DNA mass. Fluorescence intensity is in arbitrary units (x-axis) and the total number of cells is on the y-axis. (**B-C**) Graphs showing the percent G1/S-phase and G2/M-phase arrest (y-axis) for each of the 181,420 compounds (x-axis). The cutoffs for G1/S-phase inhibitors was set at >4 STDs from the average of the DMSO controls. The cutoff for G2/M-Phase inhibitors was set at >80% of the Taxol positive control average. (**D-E**) Example of compounds arresting the cell cycle in G1/S-phase and G2/M-phase and their cell cycle profiles. (**F**) Summary of screen hits. In total 30 G1/S-phase inhibitors and 483 G2/M-phase inhibitors were identified with an overall .29% hit rate. (**B-F**) see also **Table S1** & **S2**.

5.2 Antileukemic compound chemical analysis

The chemical structures and potential targets of the G1/S-phase and G2/M-phase hit antileukemic compounds were analyzed using CSNAP (Chemical Similarity Network Analysis Pulldown), our newly developed computational compound target inference program [55]. This approach compared our hit compounds to compounds within the ChEMBL database that have annotated targets and organized them into a chemical similarity network, which is composed of sub-networks made from compounds that share a similar chemotype. The chemical similarity network was then used to predict the targets of query compounds based on a scoring function (S-Score, range from 0 to 1) that takes into account the targets of known compounds in the neighborhood of query compounds. This analysis allowed us to group the 30 G1/S-phase compounds into 22 chemotype clusters and the 483 G2/M-phase compounds into 192 chemotype clusters (**Fig 5.2.1A-B** and **Table S2**). The top predicted targets for G1/S-phase inhibitors were Prothrombin and Elastase (**Fig 5.2.1C** and **Table S3**). The top predicted targets for G2/M-phase inhibitors were Tubulin and MAP Kinase (**Fig 5.2.1D** and **Table S3**). Because of our interest in

cell division, we sought to analyze the G2/M-phase network further. However, due to the overabundance of screening campaigns aimed at discovering microtubule-targeting agents, we eliminated all chemotype clusters that were predicted to be targeting microtubules (α/β-tubulin) from further consideration. This resulted in 7 remaining chemotype clusters and 31 orphan compounds that did not share significant chemical similarity to other compounds in the ChEMBL database (for example see boxed compounds in **Fig 5.2.1B**). Two compounds from each novel chemotype cluster and the 31 orphan compounds (total of 53 compounds) were selected, re-synthesized and subjected to further evaluation in secondary assays (**Table S4**).

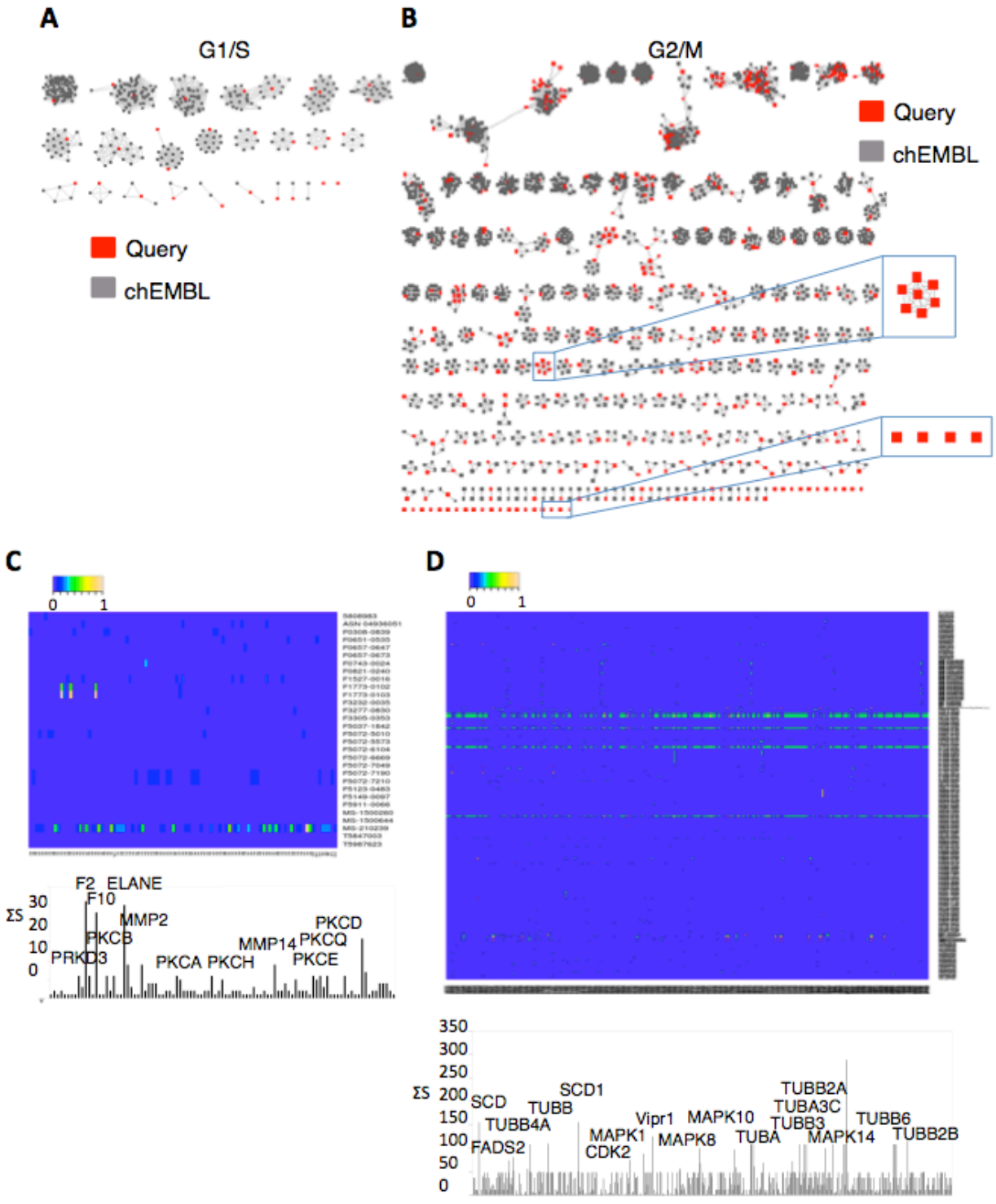

Figure 5.2.1 - Chemical analysis of leukemia G1/S-phase and G2/M-phase specific inhibitors. (**A**) CSNAP chemical similarity network of G1/S-phase inhibitors. Note that these

compounds organized into 22 chemotypic clusters and 2 compounds remained orphaned. Query compounds are in red and ChEMBL compounds are in grey. (**B**) CSNAP Chemical similarity network of G2/M-phase inhibitors. Note that these compounds organized into 192 chemotypic clusters and 31 compounds remained orphaned. Query compounds are in red and ChEMBL compounds are in grey. (**C-D**) Heatmap summaries of CSNAP S-scores, scaled from 0 to 1. The cumulative S-score (∑S-Score) of each assigned target in the target spectrum and the major predicted targets/off-targets are indicated. (**A-D**) see also **Table S3**.

5.3 G2/M-phase antileukemic compound potency

To assess the potential of the 53 selected compounds as antileukemic agents, they were tested for their ability to inhibit ALL CCRF-CEM cell viability. For viability assays, cells were treated with each compound for 72 hours and their viability was measured using the CellTiter-Glo luminescent cell viability assay (Promega), which measures total ATP levels (indicative of metabolically active cells) using a luminometer at 560 nm wavelength (**Fig 5.3.1A-B**). These assays were carried out in triplicate with a twenty-point-2-fold-titration (95.37 pM to 50 μM) for each compound, and the cell viability IC_{50} (half maximal inhibitory concentration) was derived for each compound (**Fig 5.3.1B** and **Table S4**). This analysis revealed that most compounds (51) had a cell viability $IC_{50} < 5\mu M$ (**Fig 5.3.1B** and **Table S4**).

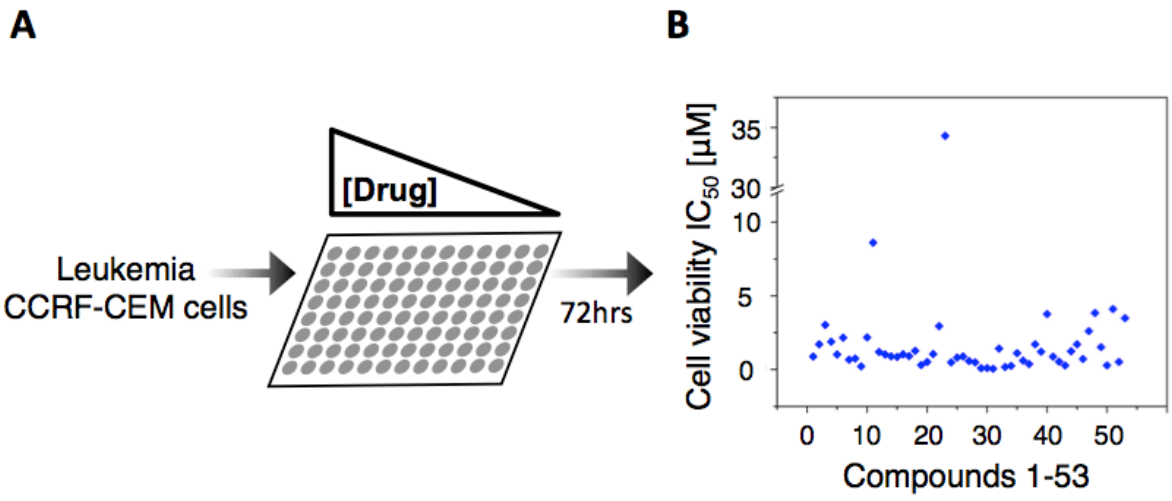

Figure 5.3.1 - Leukemia G2/M-phase inhibitor potency. (A) CCRF-CEM cells were treated with increasing concentrations of each compound for 72 hours and the cell viability was assessed using the CellTiter-Glo assay. **(B)** Summary graph showing the cell viability IC_{50} of each compound (x-axis) in µM scale (y-axis). Note that 51 compounds have cell viability IC_{50} below 5 µM. See also **Table S4**.

5.4 Multiparametric phenotypic analysis of Leukemia G2/M-phase inhibitors

To further explore the mechanism of action of G2/M-phase inhibitors, we analyzed the cellular response of cells to these inhibitors by immunofluorescence (IF) microscopy. Due to the difficulty in performing IF on CCRF-CEM cells, HeLa cells were treated with each of the 53 compounds at a concentration corresponding to their CCRF-CEM cell viability IC_{90} for sixteen hours. Cells were then fixed, permeabilized, co-stained for DNA and α-tubulin, and imaged at 63X magnification. Surprisingly, 51 compounds arrested cells with depolymerized microtubules, indicating that they were microtubule-targeting agents (**Table S4**).

Consistently, staining of the cells with a FITC fluorescently labeled antibody that recognizes the mitotic marker phosphorylated histone H3 (p-H3) [26, 56]), indicated that 51 compounds had an increased percentage of cells arrested in mitosis (% mitotic cells= number of

p-H3 positive cells/total number of cells (Hoechst DNA dye positive)) compared to controls (**Fig 5.4.1A-B**). However, two compounds, Leusin-1 and Leusin-2 (Leukemia specific inhibitors), induced a decrease in the percentage of mitotic cells and the few cells that were in mitosis displayed normal mitotic microtubule spindles (**Fig 5.4.1A-C** and **Table S4**). In HeLa cells, Leusin-1 and Leusin-2 had no effect on the mitotic microtubule spindle or interphase microtubule network, even at 137 μM for Leusin-1 or 180 μM for Leusin-2 (**Fig 5.4.1C** and **Table S2**).

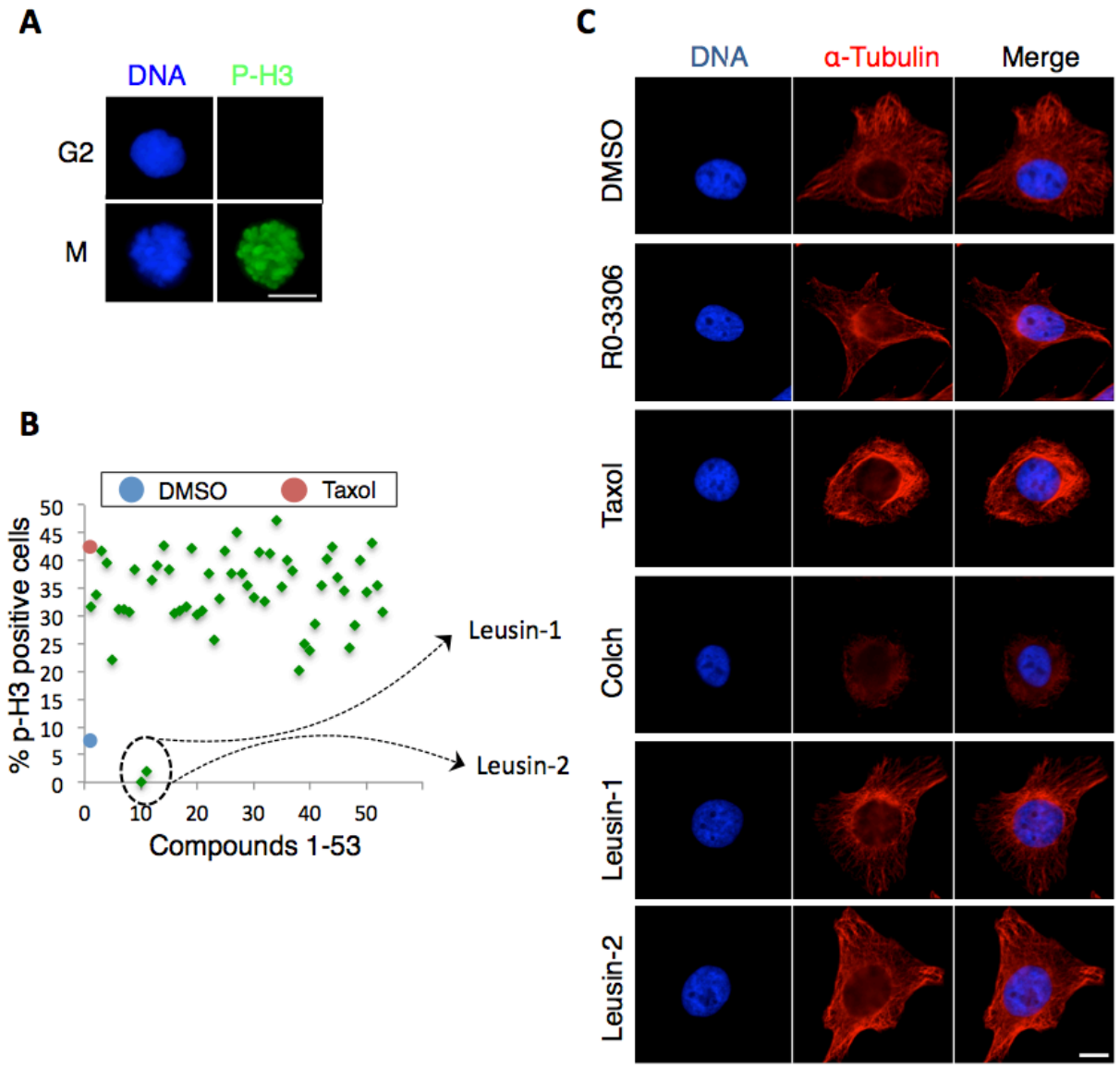

Figure 5.4.1 - Leusin-1 and Leusin-2 are G2-phase modulators. (**A**) Assay to measure percentage of mitotic cells. Cells were stained with Hoechst DNA dye (to measure total cells) and Alexa-Fluor-488-pH3 antibodies (to measure number of mitotic cells). Bar= 5μm. (**B**) Summary of the percentage of cells in mitosis (y-axis) for each of the 53 compounds (x-axis). (**C**) Immunofluorescence microscopy of HeLa cells treated with DMSO, Leusin-1, Leusin-2, Taxol, Colchicine or RO-3306 and costained for α-tubulin (anti-α-tubulin antibodies, red) and DNA (Hoechst 33342, blue). Bar= 10μm. For a summary of phenotypic classification for all 53 G2/M-phase inhibitors see **Table S4**.

Further testing of Leusin-1 and Leusin-2, in an *in vitro* microtubule polymerization assay, showed that they had no effect on microtubule polymerization, similar to the DMSO treated control (**Fig 5.4.2**). In contrast, Taxol increased the polymerization rate of microtubules and colchicine abolished microtubule polymerization (**Fig 5.4.2**). Based on their novel chemotypes and their inhibition of leukemia cell division through a G2-phase arresting and non-microtubule targeting mechanism, we selected Leusin-1 and Leusin-2 for further analysis.

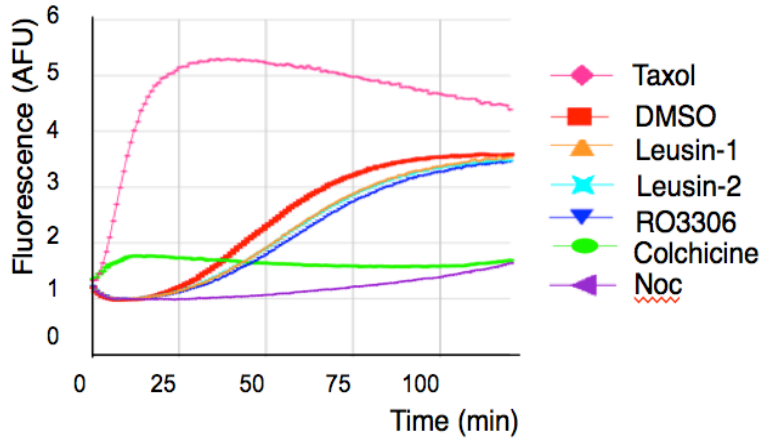

Figure 5.4.2 - Leusin-1 and Leusin-2 have no effect on microtubule polymerization. Results from *in vitro* microtubule polymerization reactions in the presence of DMSO, Taxol, RO3306, Colchicine, Nocadozole, Leusin-1, and Leusin-2. Time is in minutes (x-axis) and AFU denotes arbitrary fluorescence units (y-axis).

5.5 Leusin-1 arrest cells in G2-phase and triggers an apoptotic cell death

Due to the solubility issue of Leusin-2 chemical compound, the rest of the study was done only on Leusin-1.

Leusin-1 is a small heterocyclic molecule with drug-like properties (data not shown). To determine the consequences of arresting cells in G2-phase with Leusin-1, we analyzed the biochemical responses of cells treated with this compound. CCRF-CEM cells were treated with DMSO, Leusin-1, Thymidine (S-phase inhibitor), RO3306 (G2-phase inhibitor), or Taxol (M-phase inhibitor), and protein extracts were prepared after 16 hours. Consistent with our previous data, immunoblot analyses of protein showed that Leusin-1and RO3306-treated cells have low p-H3 (phosphorylated in mitosis), decreased level of Cyclin E, and stabilized Cyclin A and Cyclin B levels, indicative of a failure to enter mitosis. In contrast, Thymidine arrested cells with increased Cyclin E level, and decreased Cyclin A, Cyclin B, and phopho-H3 levels, means cells are blocked in S-phase. While Taxol arrested cells with increased p-H3 levels, indicative of a M-phase arrest (**Fig 5.5.1A**). Consistently, Taxol, Cisplatin, and Leusin-1 triggered the cleavage of caspase 3 indicative of apoptotic pathway activation (**Fig 5.5.1B**). Thus, cell biochemical marker analysis in response to drug treatment indicated that Leusin-1 arrests cells prior to mitosis and triggers an apoptotic cell death.

To further explore the nature of Leusin-1 induced cell death, we asked if these cells were undergoing apoptosis by analyzing the activation of effector caspases (caspase 3/7) [57]. CCRF-CEM cells were treated with DMSO, Leusin-1, or Taxol for 48 hours and the extent of caspase activation was measured using the Caspase-Glo luminescent caspase activity assay. This assay revealed that Leusin-1 was indeed inducing an apoptotic cell death similar to Taxol treatment (**Fig 5.5.1C**).

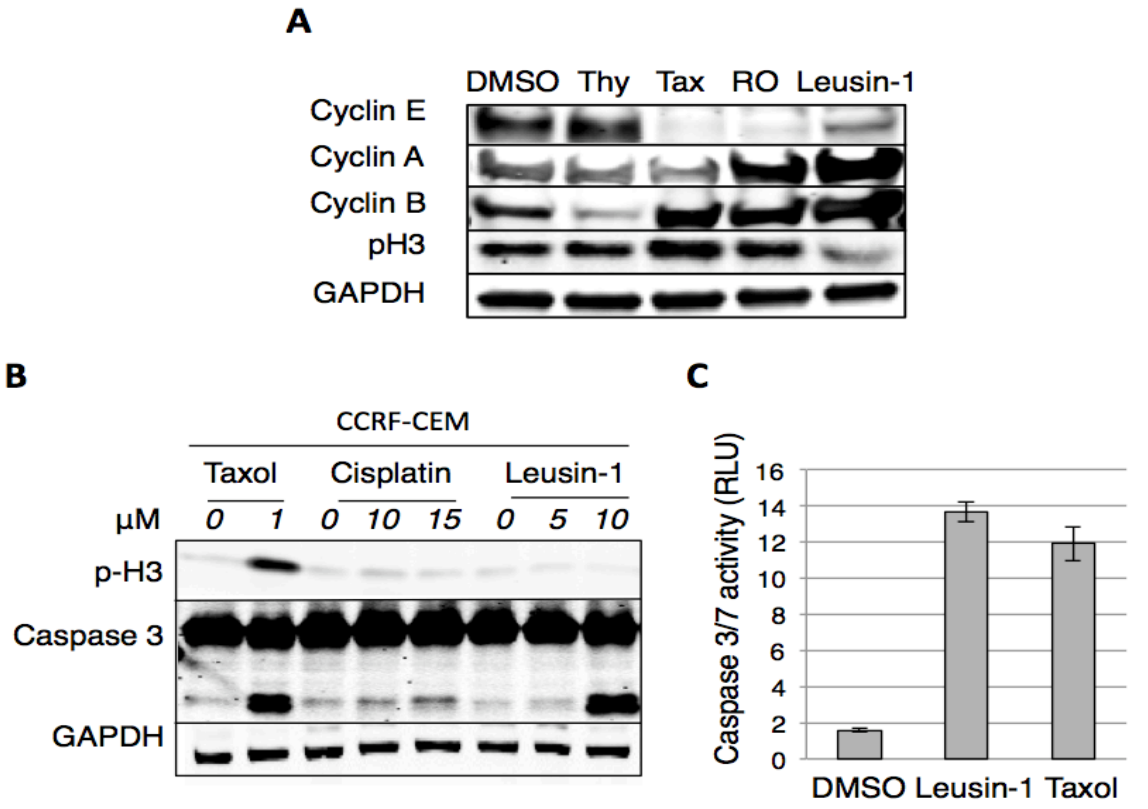

Figure 5.5.1 - Leusin-1 arrests cells in G2-phase and triggers an apoptotic cell death. (**A**) CCRF-CEM cells were treated with DMSO, Thymidine, Taxol, RO3306, or Leusin-1 for 16 hours. Extracts were prepared and immunoblotted for Cyclin E, Cyclin A, Cyclin B, phospho-H3, and GAPDH. (**B**) CCRF-CEM cells were treated with Cisplatin, Leusin-1, or Taxol for 48 hours. Extracts were prepared and immunoblotted for phospho-H3, Caspase-3, and GAPDH. (**C**) CCRF-CEM cells were treated with DMSO, Leusin-1, or Taxol for 48 hours and the Caspase 3/7 activity was quantified using the Caspase-Glo luminescent Caspase activity assay. RLU indicates relative light units. Data is presented as the average ± SD.

To further analyze the cellular consequences of treating ALL cells with Leusin-1, we performed live cell time-lapse microscopy. CCRF-CEM cells were treated with either 0.5% DMSO or 10 µM Leusin-1 for 1 hour, images were then captured at 15-min intervals for 24 hours, and processed into movie format (**Fig 5.5.2**). While DMSO treated cells progress through cell division normally, Leusin-1 treated cells showed morphological defects and eventually leads to cell apoptosis (**Fig 5.5.2**). We observed significant increasing in cell death in Leusin-1 treated

CCRF-CEM cells (80.3%) compared to DMSO control treated samples (3.7%). Our live cell time-lapse microscopy results confirmed visually that Leusin-1 was able to induce cell death.

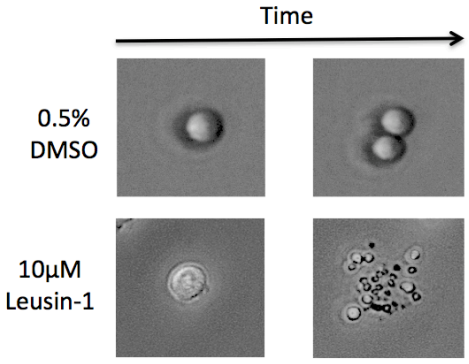

Figure 5.5.2 - Leusin-1 induces cell apoptosis. Live cell time-lapse microscopy of CCRF-CEM cells treated with DMSO, or Leusin-1. Time is in hours.

5.6 Leusin-1 is an ALL specific inhibitor

To determine whether Leusin-1 was active against a broad array of cancer or was specific for leukemia, we treated a diverse panel of cancer cell lines and normal cell lines with Leusin-1 for 72 hours. These included cervical adenocarcinoma (HeLa), breast adenocarcinoma (MCF7), melanoma (M233), osteosarcoma (U2OS), non-small cell lung carcinoma (NCI-H460), acute lymphoblastic leukemia (CCRF-CEM), retinal pigment epithelial cells (hTERT-RPE), Lymphoma (Jeko-1), and colorectal carcinoma (HCT 116). The cell viability IC_{50} was then quantified and compared to the DMSO control (**Fig 5.6.1A**). Interestingly, Leusin-1 showed greater specificity for CCRF-CEM cells compared to all other adherent types of cancers (CCRF-CEM cell viability IC_{50} for Leusin-1= 2.64 μM, compared to 4-50 fold for all other cell lines) (**Fig 5.6.1A** and **Fig S7**). To determine if Leusin-1 was active against all leukemia or only a subset of leukemia, we analyzed the efficacy of Leusin-1 in a panel of leukemia cell lines. These included ALL (CCRF-CEM and TOM-1), AML (HL-60 and THP-1), and CML (K562 and KCL22) leukemia cell lines. Surprisingly, ALL cell lines were more sensitive to Leusin-1 (for

Leusin-1 CCRF-CEM IC_{50}= 2.66 µM and TOM-1 IC_{50}= 0.877 µM, compared to 5-30 µM for all other leukemia cell lines (**Fig 5.6.1B** and **Fig S8**). These results indicated that Leusin-1 is an ALL specific inhibitor. In comparison to the other leukemia inhibitors in the clinic or FDA approved for the treatment of leukemia (like vinblastine), Leusin-1 had a much greater specificity indicating a potential for a more favorable therapeutic window.

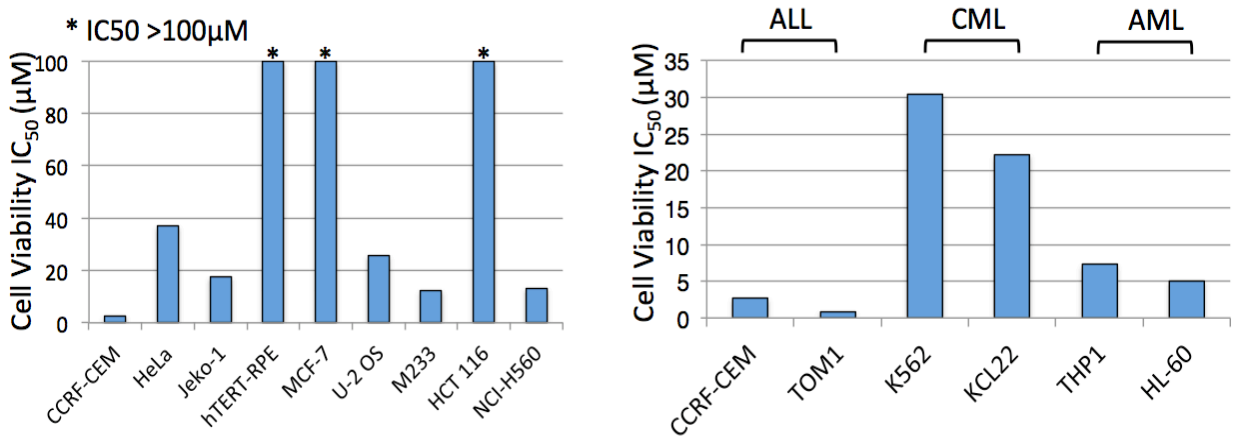

Figure 5.6.1 - Leusin-1 is ALL specific. (**A**) A broad panel of cancer cell lines was treated with increasing concentrations of Leusin-1 for 72 hours and their cell viability IC_{50} was assessed using the CellTiter-Glo assay. Graph shows summary of results for cell viability IC_{50} (y-axis) for each cell line (x-axis). (**B**) A panel of Leukemia cells was treated with increasing concentrations of Leusin-1, and the cell viability IC_{50} (y-axis) was determined for each cell line (x-axis). ALL (CCRF-CEM and TOM-1); CML (K562 and KCL22); and AML (HL-60 and THP-1).

5.7 Leusin-1 inhibits ALL colony formation

Finally, we assessed the ability of Leusin-1 on inhibiting CCRF-CEM colony formation using a clonogenic assay (**Fig 5.7.1A**). Significant differences in long-term survival were detected after 18 days of incubation with 2 µM of Leusin-1, compared to the DMSO control cells. Colonies composed over 30 cells are scored, and all values are normalized to the average

of DMSO treated cells. Leusin-1 treatment abolishes colony formation comparable to Taxol positive control (**Fig 5.7.1B**).

Alternatively, we also measured the anchorage-independent growth of CCRF-CEM cells upon drug treatment using a fluorescence based transformation assay. Consistent with clonogenic assay, Leusin-1 treated cells have dramatic reduction in cell transformation compare to the DMSO control (**Fig 5.7.1C**). This implies that Leusin-1 can inhibit anchorage-independent growth and colony formation upon prolonged incubation with ALL CCRF-CEM cells.

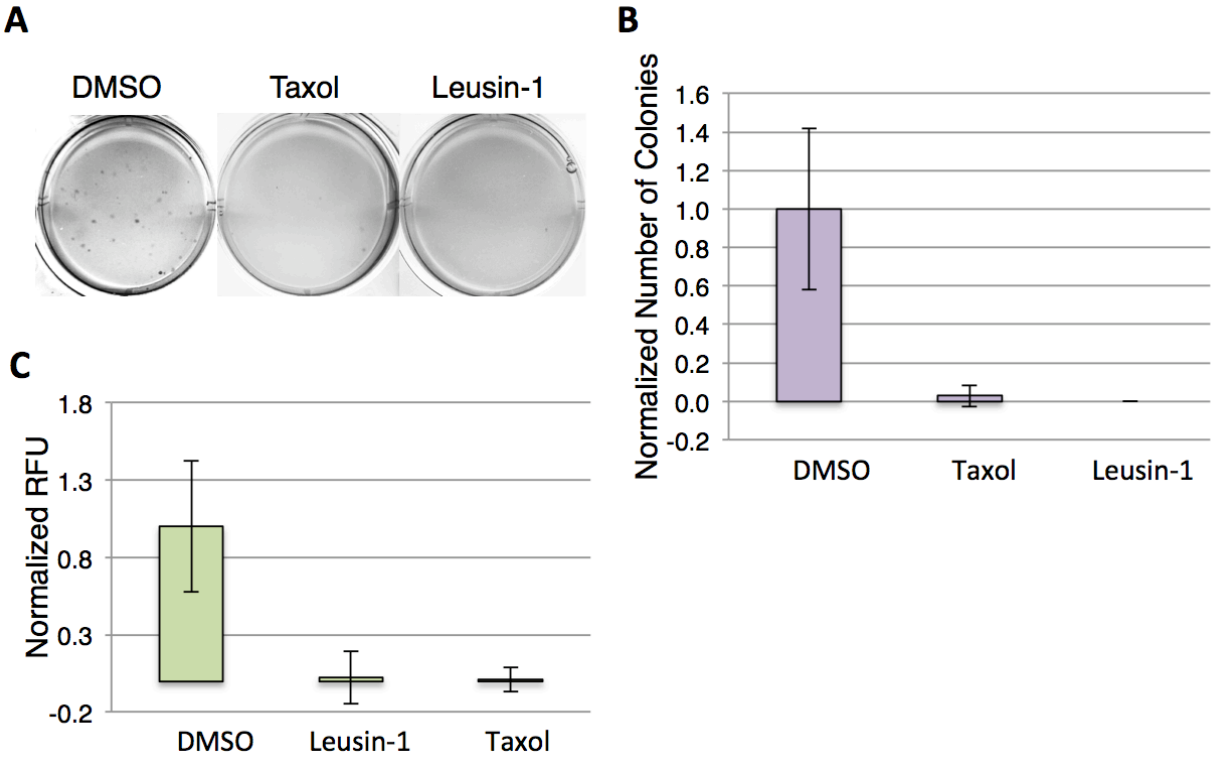

Figure 5.7.1 - Leusin-1 inhibits ALL colony formation. (**A-B**) CCRF-CEM cells were treated with DMSO, Leusin-1, or Taxol for 18 days and the percent colony formation, normalized to DMSO, was quantified. Data is represented as the average percent ±SDs. (**C**) ALL transformation assay. ALL CCRF-CEM cells were cultured for 14 days in complete medium containing soft agar and indicated concentration of DMSO, Leusin-1, or Taxol. Fluorescent signals that are proportional to cell numbers are measured and normalized to DMSO control.

CHAPTER 6 – FUTURE DIRECTIONS

The selection of Leusin-1 as a lead antileukemic compound in our study highlights the utility of suspension cell-based chemical screening for the identification of cell permeable, drug-like, and cell cycle-phase specific drugs. Leusin-1 arrests cells in the G2-phase of the cell cycle, leads to apoptosis, has broad anti-cancer activity, and is especially potent against ALL. In addition, this integrated approach of high throughput screening platform utilizing cell cycle profiling, computational chemoiformatics, potency in cells, and multiparametric phenotypic analysis, can be served as a strategic template for identification small molecule cell cycle modulators in suspension cells. Last but not least, this study has generated a wealth of novel compounds that targets specific cell phases and represent variable chemotypes, which warrant further evaluation and characterization as antileukemic agents.

To further elucidate Leusin-1's ALL specific nature, and understand its mechanism on G2-phase inhibition, we would like to:

6.1 Identify the molecular target of Leusin-1

Interestingly, our data indicated that Leusin-1 was not targeting the frequently drugged ALL targets like DNA replication/repair (no pH2AX staining) (data not shown), proteasome dependent degradation (G2-phase arrest versus an arrest at the metaphase to anaphase transition) (**Fig 5.5.1A**), and Aurora A or B activity (G2-phase arrest versus M-phase arrest, also Aurora B inhibition eliminates p-H3) (**Fig 5.5.1A**) [58]. Additionally, chemical analysis of Leusin-1 showed that it did not resemble any of the 37 known ALL inhibitors in the clinic [58]. Thus, it is likely that Leusin-1 is targeting new proteins critical for ALL cellular survival. The

identification of the molecular target will be critical to the future development of Leusin-1 for therapeutic purposes.

Drug Affinity Response Target Stability (DARTS)

To start, we first sought to use Drug Affinity Response Target Stability (DARTS) to identify the molecular target of Leusin-1. DARTS takes advantage of a reduction in the protease susceptibility of the target protein upon drug binding [59]. The procedure for DARTS involves treating CCRF-CEM whole cell lysate with either Leusin-1or DMSO control, then the samples will be digested with varying amounts of protease and ran on 1D SDS–PAGE, staining the gel with Coomassie Blue, and analyzing the respective lanes of the gel for bands that are more intense in drug treated sample over the control sample. Upon finding a band whose abundance differs between the Leusin-1-treated and DMSO control-treated samples, each band can be cut out, digested with trypsin, and analyzed by liquid chromatography coupled to tandem mass spectrometry (LC−MS/MS). After annotating the peptides and proteins identified in each gel band, label-free quantitative analysis using spectral counting, LC/MS extracted ion currents (XIC), or MS/MS total ion current (TIC) can determine which identified protein has been enriched in the DARTS experiment [60, 61].

Upon identification of the protein targets, we will validate them by using Isothermal Titration Calorimetry (ITC) [62]. ITC measures the binding equilibrium directly by determining the heat evolved on association of a ligand with its binding partner, and can determine the binding affinity (Ka), enthalpy changes (ΔH), and binding stoichiometry (n) of the interaction between two or more molecules in solution. This *in vitro* study will confirm direct binding

between Leusin-1 and its protein target before we dissect the mechanism of action further *in vivo*.

After we performed protease digestion on Leusin-1 treated or DMSO control treated CCRF-CEM cell lysate, we didn't observe any protein abundance difference on either Coomassie Blue stained or silver stained SDS-PAGE gel. This in fact, is one shortcoming of the DARTS method, if the target protein could either not be sufficiently abundant in the cell to be visibly stained, or even if it is abundant enough to see, its enrichment in one sample over another could be masked because the protein comigrates with many other proteins of the same molecular weight on the gel [63], then it won't be a feasible method for protein target identification.

Chemical Similarity Network Analysis Pulldown (CSNAP)

With the initial unfruitful attempt of DARTS, we then turn to CSNAP analysis again with lower stringency to see if there is any compounds in CHEMBL database that shares similar chemical structure and has a known target [55]. Initially, we used a scoring function (S-score, range from 0-1) to score target assignments by counting the target annotation frequency in the nearest neighborhood of query compounds. After lowering cutoff score from 0.8 to 0.7, we identified several putative protein targets. Among these, X-box binding protein 1 (XBP-1) and Bromodomain adjacent to zinc finger domain 2B (BAZ2B) caught our attention, as these proteins have established role in ALL and leukemia in general [64, 65].

To follow up on XBP-1, we induced UPR response of CCRF-CEM cells by the addition of Tunicamycin and treated with Leusin-1 at the same time, then looked for whether Leusin-1 affects XBP-1 protein expression using immunoblot after 16 hours. The XBP-1 protein is a transcription factor that regulates the expression of genes in the cellular stress response, and it is

spliced by IRE1 endoribonuclease upon sensing unfolded proteins [66, 67]. This splicing event results in the conversion of a 267- amino acid XBP-1u encoded by unspliced XBP-1 mRNA to a 371-amino-acid XBP-1s by spliced XBP-1 mRNA in murine cells. XBP-1s then translocates into the nucleus, where it binds to its target sequence in the regulatory regions of the chaperone genes to induce their transcription [66, 67]. Only the spliced form of the XBP-1s protein is an active transcription factor, while XBP-1u has no transactivation ability. If Leusin-1 were an inhibitor for XBP-1s, then we would expect XBP-1s expression level not affected by the addition of Leusin-1. Our immunoblot showed Tunicamycin was able to induce XBP-1s protein expression level consistent with previous finding, but addition of Leusin-1 decreased Tunicamycin-induced XBP-1s expression. This leads us to hypothesize that Leusin-1 might inhibit XBP-1u or the splicing event of XBP-1s. To test this, we performed Real-Time Quantitative Reverse Transcription PCR (RT-PCR) to exam gene expression alteration of several UPR target genes that are known to be regulated by XBP-1. We tested for EDEM and CHOP, EDEM is dependent on XBP-1 for Tm-induced expression, while CHOP gene expression is XBP-1s independent [68]. However, our RT-PCR results did not show such effects. Combining the evidences from immunoblot of XBP-1 splicing and RT-PCR for target gene expressions, we ruled out that XBP-1 is the target for Leusin-1.

On the other hand, we tested BAZ2B as the potential target for Leusin-1 using proteolysis protection assay and ITC. Bromodomains are acetyl-lysine specific epigenetic reader domains and an emerging new target class for the design of protein interaction inhibitors that selectively modulate gene transcription [69]. Recently, the first inhibitors target the Bromo and Extra-Terminal (BET) subfamily of bromodomains have reached clinical testing [70]. While Bromodomain adjacent to zinc finger domain (BAZ) subfamily are less studied, and only two

inhibitors have been reported with unknown cellular function [64, 71]. Interestingly, BAZ2B gene locus have been identified to be associated with sudden cardiac death, and high expression levels of BAZ2B have found to be associated with poor outcome of pediatric B cell acute lymphoblastic leukemia (B-ALL) [64, 72]. This leads us to explore the potential that Leusin-1 acts as an inhibitor for ALL through interaction with BAZ2B. We incubated Leusin-1 or DMSO with purified His-tagged BAZ2B Bromodomain protein for 1 hour at room temperature with light shaking, then subjected the mixture to proteolysis by Pronase for 1.5 hour at 4°C. After digestion, we run samples on SDS-PAGE, and stained with Coomassie Blue to visualize the stabilization of BAZ2B Bromodomain upon Leusin-1 treatment. Our preliminary data showed that BAZ2B protein indeed is protected and stabilized by Leusin-1 (**Fig 6.1.1**). With this initial confirmation, we examined further using ITC to establish direct binding of BAZ2B and Leusin-1. Our preliminary data indicated that BAZ2B only weekly associated with Leusin-1 (data not shown).

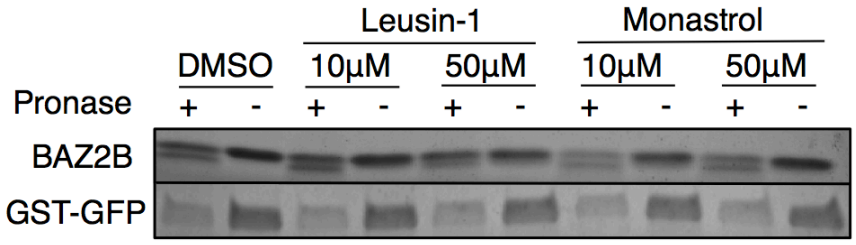

Figure 6.1.1 - Leusin-1 protects BAZ2B from proteolysis. BAZ2B or GST-tagged GFP protein are incubated with DMSO, indicated concentrations of Leusin-1, or indicated concentrations of Monastrol for 1 hour at room temperature with light shaking. The mixtures are subjected to proteolysis by Pronase for 1.5 hour at 4°C with shaking. After digestion, samples were ran on SDS-PAGE, and stained with Coomassie Blue. Note that Monastrol treated samples are served as negative control for small molecule protein binding control, and GST-tagged GFP samples are served as specific protection of Leusin-1 over BAZ2B protein negative control.

With BAZ2B being only weakly associated with Leusin-1, we sought to test the interaction between BAZ2A and Leusin-1. BAZ2A shares very similar Bromodomain structure as BAZ2B, and the existing inhibitors of BAZ2 A/B binds to both proteins at very similar K_D [64, 71]. BAZ2A forms the nucleolar remodeling complex (NoRC), and NoRC has been shown to regulate expression of noncoding RNAs and also establishes a repressive heterochromatic structure at centromeres and telomeres [73, 74]. Interestingly, BAZ2A expression has been shown to be correlated with recurrence in prostate cancer [75]. We are currently trying to express and obtain recombinant BAZ2A protein through purification, and will again run ITC on BAZ2A with Leusin-1 as we did for BAZ2B.

Functional Genomic Screen

As an alternative, we could also perform genome-scale shRNA screens to identify the mechanism of action of Leusin-1. With the recent availability of ultracomplex shRNA libraries that target the entire human genome with ~25 shRNAs per gene and contain thousands of negative control shRNAs, allows significantly reduction of both false-negative and false-positive rates [76]. This approach that coupled a phenotypic small molecule screen with a functional genomic screen to identify mechanism of action, has recently led to the discovery of a highly specific inhibitor of nicotinamide phosphoribosyltransferase gene (NAMPT) [77] . The lead compound, STF-118804, has been shown to be active in mouse model of leukemia, and had no appreciable toxicity in the mouse. Thus, we believe genome-scale shRNA screen could be very useful in identifying the mechanism of action for Leusin-1.

6.2 Test Leusin-1's potency in primary patient cell lines

We have previously showed a specificity of Leuin-1 over other cancer types, and ALL over other leukemia types (**Fig 5.6.1A-B**). To carry this to the next step, we will collaborate with Kelliher lab from University of Massachusetts Medical School on testing Leusin-1 on a panel of primary pediatric and adult ALL cell lines. They have demonstrated a dependency of ALL on antiapoptotic protein (BCL-2, BCL-XL) using this panel of pediatric and adult patient-derived cell lines [78]. Having access to those clinically obtained primary cell lines would allow us to test specificity demonstrated by increased potency of Leusin-1 in ALL over other leukemia, a difference in pediatric versus adult ALL, and ETP-ALL subgroup that has a very high risk for relapse, in a clinical relevant setting [78].

CHAPTER 7 – MATERIAL AND METHOD

7.1 Cell culture

CCRF-CEM and HeLa cell lines were purchased from ATCC, which verified identity by short-tandem repeat profiling, were passaged for less than 2 months following receiving and were maintained in RPMI1640 medium (GIBCO) with 10% FBS, 2 mM L-glutamine and antibiotics, in 5% CO_2 at 37^{o} C.

7.2 High-throughput screening

Screening conditions were as described previously [79] with the following minor modifications. CCRF-CEM cells were plated in 384-well plates (1,000 cells/well) and treated with 10μM drugs for 16 hours. Cells were fixed and stained with 2.5 μM Vybrant DyeCycle Green (Invitrogen) for 3 hour at room temperature and plates were scanned with an Acumen ^{e}X3 (TTP Labtech) fluorescence cytometer using its 488 nm laser and a cell cycle histogram profile was generated for each well. For the G2/M-phase secondary screen, 16 hours post drug addition cells were fixed with 4% paraformaldehyde, permeabilized with 0.1% Triton X-100/PBS and stained with Alexa-488-phospho-histone-H3 (Ser10, Cell Signaling) and 0.25 μg/ml Hoechst 33342 for 1 hour. Plates were washed twice with PBS using a microplate washer (BioTek), then imaged with an ImageXpress Micro (Molecular Devices) high-content fluorescence microscope. Data analysis was performed using the CDD (Collaborative Drug Discovery) software and outputs were exported to Excel.

7.3 CSNAP chemical analysis

CSNAP was used to predict the targets of G1/S-phase and G2/M-phase inhibitors as described previously [55]. Briefly, compounds were queried in the annotated ChEMBL database version 18 using the following search parameters: Tanimoto cutoff= 0.75, z-score cutoff= 2.5. The ChEMBL target annotations were retrieved from the database based on the following criteria: confidence score= 4, assay-type= binding. Finally, chemical similarity networks and ligand-target interaction fingerprints (LTIFs) analyses were analyzed using Cytoscape and the R statistical package respectively.

7.4 Compound potency

For cell viability IC_{50}s, cells were treated with a twenty-point-2-fold-titration (95.37 pM to 50 μM)). Cell viability IC_{50}s were determined using the CellTiter-Glo Assay (Promega), which measures total ATP levels. Plates were read with a Tecan M1000 micro-plate reader at 540nm and CDD software was used for generating IC_{50} and IC_{90} values.

7.5 Immunofluorescence and time-lapse microscopy

Immunofluorescence microscopy was carried out as described in [13]. Except that images were captured with a Leica DMI6000 microscope (Leica Microsystems) and deconvolved with Leica deconvolution software. Time-lapse microscopy was performed as described in [26]. Briefly, CCRF-CEM cells were treated with indicated drugs or control DMSO for 1 hour, then ten Z-stack images (0.9μm steps) were captured at 15-minute intervals for 24 hours. Images were deconvolved and converted to AVI movie files.

7.6 Apoptosis assay

CCRF-CEM cells were treated with indicated drugs for 48 hours and the Caspase-Glo luminescent caspase activity assay (Promega) was used to measure the activity of effector caspases, as a read-out of apoptosis. Plates were scanned with a luminometer at 520 nm wavelength and the apoptotic index (total caspase activity/total number of cells) per well was measured. Quantitation is in relative light units (RLU) compared to DMSO control.

7.7 Leukemia clonogenic assay

5,000 CCRF-CEM cells/well were grown in 6-well plates with semisolid RPMI1640 medium containing 10% FBS, 0.45% agarose, and drug (2 μM Leusin-1, 2 μM Leusin-2, 1%DMSO, or 50 nM Taxol). A layer of 500 μl of medium containing the corresponding drug was added on top and plates were incubated in 5% CO_2 at 37^{o} C for 3 weeks. Fresh medium were replenished twice a week. Colonies (>30 cells) were scored and visualized after the addition of 0.005% crystal violet overnight.

7.8 Leukemia transformation assay

CytoSelect™ 96-Well Cell Transformation Assay kit (Cell Biolabs, Inc.) was used for assessing soft agar colony formation following the manufacturer's instructions. Fluorescent signals from Leusin-1, Leusin-2, or Taxol treated cells were normalized with the average of DMSO control after subtracting the value from the no cell blank, and the normalized data were plotted.

7.9 *In Vitro* Tubulin polymerization assay

Tubulin polymerization reactions were carried out according to the manufacturer's instruction (Cytoskeleton, BK011P) in the presence of DMSO or 3 μM Leusin-1, Leusin-2, Taxol or colchicine. Polymerization was monitored with a Tecan M1000 micro-plate reader at 420 nm for 120 minutes at 37°C**.**

7.10 Antibodies

Phospho-histone-H3-Alexa-Fluor-488 (Ser10) (Cell Signaling cat# 3465); α-tubulin (Serotec cat# MCAP77G); Gapdh (Covance cat#MMS-580S), α-tubulin (Serotec cat#MCAP77), Caspase 3 (Cell Signaling Technology cat#9665), cyclin A (Santa Cruz Biotechnology cat#SC-751), cyclin B1 (Santa Cruz Biotechnology cat#SC-245), cyclin E (Cell Signaling Technology cat#4129P), XBP-1 (Millipore 09-722), XBP-1S (Proteintech 24868-I-AP); Cy3-conjugated secondary antibodies is from Jackson Immuno Research.

7.11 Statistical analysis

The quality of the screen was assessed by calculating the Z' factor (Z' factor = 1-3 x $(\sigma_p+\sigma_n)/(|\mu_p-\mu_n|)$), which takes into account the dynamic range of the assay and variance of the data [80]. The screen performed with an average plate Z' factor of 0.48 ± 0.06, close to the optimal performance range of 0.5-1 [80].

7.12 Drug Affinity Response Target Stability (DARTS)

DARTS was performed by either using CCRF-CEM cell lysate, or recombinant proteins (GST-GFP or BAZ2B). Hela cell lysate (500μg) was incubated with 500μM Leusin-1 or control

DMSO in TNC buffer at room temperature for 1 hour [59]. Thermolysin (1:25 wt:wt, Thermolysin:cell lysate) was then added to the drug lysate mix and incubated 1.5 hours at 4°C. The mixture and then denatured and ran on SDS-PAGE and stained with Coomassie Blue or silver stain (Biorad 161-0449). Recombinant BAZ2B is used in a separate experiment by incubate 2.0μg purified BAZ2B protein or purified GST-GFP protein with indicated drug and control at room temperature for 1 hour. Then Pronase (1:100 wt:wt, Pronase:XBP-1) was used for proteolysis following the same procedure.

7.13 Isothermal Titration Calorimetry (ITC)

All calorimetric titration experiments were carried out on MicroCal iTC200 at 25℃. The buffer condition used was 50 mM Tris-HCl, 100 mM NaCl, 0.04% Tween 20, 20% Glycerol, pH 8.0. Titration was performed by injecting the either BAZ2B proteins (300 mM) into a reaction cell containing the 20mM of either DMSO, Leusin-1, or GSK2801. Integrated heat of the titrations after corrected for the heat of dilution were analyzed using the Origin program. The corrected data were fitted to a single binding site model using a nonlinear least-square minimization algorithm, and the binding parameters including reaction enthalpy changes (ΔH), reaction enthalpy changes (TΔS), equilibrium dissociation constants (K_D), stoichiometry (n) were calculated.

CHAPTER 8 – SUPPLEMENTAL TABLES AND FIGURES

Table S1 – Screening Summary

Category	Parameter	Description
Assay	Type of assay	Cell-based (CCRF-CEM, pediatric ALL cell line)
	Target	Cell cycle modulators
	Primary measurement	Cell cycle profile, detection of G1/S, G2/M arrest
	Key reagents	Vybrant DyeCycle Green Stain, p-H3-488 antibody
	Assay protocol	See material and method
Library	Library size	181,420
	Library composition	Drug-like small molecule
	Source	UCLA Molecular Screening Shared Resource
Screen	Format	384-well plate
	Concentration tested	10 μM, <1% DMSO
	Plate controls	Internal controls DMSO, Taxol
	Reagent/compound dispensing system	Biomek FX (Beckman Coulter)
		and Multidrop 384 liquid handlers (Thermo LabSystem)
	Detection instrument and software	Acumen eX4 (TTP Labtech)
	Assay validation/QC	Z' score 0.48 ± 0.06
	Normalization	To inter-plate controls DMSO and Taxol
Post-HTS analysis	Hit Criteria	G1/S-phase inhibitors (>4 STDs from inter-plate DMSO control)
		G2/M-phase inhibitors (>80% of inter-plate Taxol control)
	Hit rate	Total cell cycle modulator hit rate = 0.29%
		G1/S-phase inhibitors hit rate = 0.017%
		G2/M-phase inhibitors hit rate = 0.27%
	Additional assays	G2/M deconvolution screen for p-H3-488 positive cells
		CellTiter-Glo luminescent cell viability assay
		Immunofluorescence microscopy-based phenotypic analysis
	Confirmation of hit purity and structure	Compounds were repurchased from MolPort and compound
		structure and purity were verified analytically

Table S2 – Summary of G1/S Leukemia cell cycle inhibitors

	Molecule Name	No. of St Dev above DMSO
1	F0657-0647	10.35
2	F5072-5010	10.19
3	F0657-0673	9.83
4	MS-1500260	9.54
5	F5072-7210	9.43
6	F0308-0839	9.42
7	F5072-7190	9.34
8	F3232-0035	9.29
9	F5911-0066	9.24
10	F0651-0535	9.08
11	F5072-5573	8.91
12	F1773-0103	8.73
13	MS-1500644	8.22
14	F1527-0016	7.70
15	F5072-7049	7.44
16	F3305-0353	6.86
17	F5072-6669	6.47
18	T5987623	6.31
19	F1773-0102	6.28
20	F0743-0024	5.64
21	F5072-6104	4.69
22	F3277-0830	4.63
23	ASN 04936051	4.28
24	5808983	4.23
25	T5847003	4.16
26	F5123-0483	3.92
27	F5037-1842	3.81
28	F0821-0240	2.73
29	MS-210239	2.68
30	F5149-0097	2.30

Table S3 – Summary of G2/M Leukemia cell cycle inhibitors

	Molecule Name	Percentage G2/M normalized to Taxol
1	F2093-0051	117.41
2	F1298-0926	113.81
3	ASN 04053495	111.00
4	F2487-0352	110.54
5	F2481-0446	110.20
6	F1015-0297	109.90
7	F0193-0287	109.75
8	F3225-8496	109.71
9	F0187-0071	109.60
10	F2269-0014	109.50
11	F6195-5713	109.14
12	F1848-0114	109.04
13	F2506-1309	108.97
14	ASN 05545956	108.93
15	F2211-0050	108.85
16	F2503-0097	108.81
17	F2210-0032	108.40
18	MS-1504410	107.94
19	ASN 05543939	107.82
20	F5835-0223	107.61
21	ASN 05548429	107.57
22	F3167-0372	107.54
23	F3296-0190	107.39
24	F5578-1662	107.14
25	F5871-3531	107.09
26	F5001-1073	106.96
27	F2269-0119	106.94
28	F5001-0898	106.85
29	F3222-2226	106.65
30	F3294-0072	106.57
31	F5097-1165	106.56
32	F5001-0724	106.26
33	F2616-0891	106.23
34	F5686-0860	106.23
35	5194550	106.13
36	F5097-1181	106.11
37	F5097-1115	106.03
38	F0440-0186	106.01
39	F2487-0240	105.99
40	F0344-0966	105.96

Table S3 – Continued from previous page

	Molecule Name	Percentage G2/M normalized to Taxol
41	F0526-2190	105.93
42	F3406-4686	105.91
43	F2269-0551	105.87
44	F2336-0042	105.77
45	F2555-0093	105.70
46	ASN 06018762	105.65
47	T5734552	105.55
48	F3398-5051	105.40
49	F5834-4825	105.39
50	T6092696	105.38
51	F3406-0765	105.31
52	F0280-0213	105.28
53	F5834-4837	105.27
54	F2555-0089	105.20
55	F3406-4697	105.19
56	ASN 05588736	105.16
57	F0344-1092	105.14
58	F6195-2790	105.09
59	ASN 05397535	105.08
60	F1793-0013	105.03
61	F2701-0400	104.98
62	5728294	104.94
63	F5086-0795	104.89
64	F3244-0338	104.87
65	F1298-0844	104.80
66	F0196-0158	104.79
67	F1757-0071	104.77
68	F1298-0936	104.70
69	F1298-0413	104.68
70	F2147-0712	104.64
71	F3225-8497	104.63
72	ASN 05548536	104.63
73	F0440-0063	104.61
74	F3237-0694	104.57
75	F0060-0164	104.57
76	F3406-4695	104.56
77	ASN 04371226	104.54
78	F0016-0887	104.49
79	F0526-2154	104.44
80	Colchicine	104.38

Table S3 – Continued from previous page

	Molecule Name	Percentage G2/M normalized to Taxol
81	F2373-0040	104.37
82	F0651-0159	104.36
83	6641425	104.35
84	F5686-0844	104.33
85	5784148	104.24
86	F5001-0052	104.23
87	F5097-1172	104.22
88	F0012-0274	104.22
89	F3406-0765	104.18
90	F1787-0618	104.15
91	5175570	104.13
92	F2663-0020	104.11
93	F1803-0039	104.08
94	F0174-0041	104.06
95	F0349-4744	104.05
96	MS-1505328	104.02
97	F5097-1186	103.99
98	ASN 02254668	103.96
99	F1822-0098	103.93
100	ASN 05588738	103.93
101	F2554-0177	103.88
102	SAM002699893	103.85
103	F2158-0029	103.83
104	F0697-0151	103.83
105	ASN 05548730	103.79
106	F5001-1582	103.78
107	F0700-0126	103.73
108	F3382-0246	103.72
109	Parbendazole	103.63
110	F2964-1887	103.62
111	ASN 05588326	103.61
112	F0882-1027	103.54
113	F1298-0844	103.53
114	F3379-0117	103.50
115	F0344-0975	103.46
116	ASN 03849556	103.43
117	F1015-0327	103.43
118	F2493-0851	103.42
119	F3222-4636	103.40
120	F6195-2957	103.39

Table S3 – Continued from previous page

	Molecule Name	Percentage G2/M normalized to Taxol
121	F3318-0114	103.34
122	5338490	103.31
123	F2382-0143	103.24
124	5625039	103.22
125	ASN 05988752	103.18
126	F2382-0144	103.18
127	F3406-5077	103.13
128	F1298-0357	103.12
129	5302781	103.07
130	ASN 07462031	103.07
131	F5032-0017	103.05
132	T5855297	103.04
133	F2506-1203	103.04
134	F1808-0112	103.03
135	F2269-0004	102.99
136	F1897-0333	102.95
137	ASN 04395043	102.95
138	F1298-0324	102.94
139	F0016-0389	102.93
140	ASN 03800305	102.86
141	F2650-0155	102.79
142	F2410-0978	102.73
143	F1109-0157	102.69
144	F5893-0216	102.63
145	F0161-0377	102.61
146	F3406-1010	102.54
147	F1298-0372	102.53
148	Chelidonine monohydrate (+)	102.51
149	F0777-2111	102.51
150	F2416-0497	102.41
151	F2493-3468	102.38
152	F5097-1201	102.37
153	ASN 05588743	102.35
154	F2633-0013	102.33
155	ASN 05547057	102.27
156	F0014-0323	102.22
157	Colchicine	102.15
158	F2269-0540	102.15
159	F0344-0980	102.13
160	ASN 03800266	102.08

Table S3 – Continued from previous page

	Molecule Name	Percentage G2/M normalized to Taxol
161	ASN 05548668	102.05
162	F2211-0114	102.01
163	F1298-0847	102.00
164	F5119-0499	102.00
165	T6147101	101.98
166	5576046	101.98
167	T5826904	101.93
168	ASN 04394944	101.91
169	ASN 06117349	101.89
170	F2574-0528	101.88
171	F1639-0146	101.86
172	5651851	101.85
173	T5728815	101.80
174	5301107	101.78
175	SAM001246568	101.77
176	F5834-4832	101.76
177	F3382-7868	101.73
178	F2210-0026	101.70
179	F5119-0499	101.67
180	T5926655	101.57
181	F3385-3547	101.49
182	F1298-0323	101.46
183	F2580-0543	101.41
184	F3385-3038	101.33
185	T5906514	101.30
186	F3406-5050	101.27
187	F3406-0773	101.26
188	5262045	101.22
189	F1298-0845	101.20
190	5705511	101.15
191	5754791	101.12
192	ASN 01843123	101.05
193	F0016-0542	100.99
194	F1803-0039	100.95
195	F2580-0102	100.92
196	F0344-0918	100.89
197	5666619	100.82
198	T5730868	100.82
199	F1298-0324	100.78
200	F2478-0089	100.78

Table S3 – Continued from previous page

	Molecule Name	Percentage G2/M normalized to Taxol
201	T6067163	100.76
202	AST 5940462	100.73
203	T6126001	100.68
204	5380449	100.65
205	5227882	100.63
206	F2633-0020	100.60
207	F3158-0129	100.60
208	Methiazole	100.55
209	F0440-0185	100.49
210	F2555-0177	100.49
211	T6102750	100.43
212	F0672-0673	100.43
213	F2580-0556	100.36
214	F5834-4836	100.35
215	F2991-0225	100.31
216	F1298-0322	100.30
217	F2633-0008	100.29
218	F3398-1409	100.26
219	F3406-1010	100.25
220	F2269-0520	100.21
221	5805998	100.20
222	F5001-0897	100.19
223	ASN 05944549	100.19
224	F3398-0920	100.17
225	F3406-5142	100.16
226	ASN 05548609	100.14
227	F3166-0114	100.12
228	ASN 04394980	100.11
229	F3398-0924	100.10
230	F3260-0796	100.07
231	SAM001246689	100.04
232	F0012-0270	100.01
233	T5738394	100.01
234	F5228-1317	99.98
235	5784156	99.96
236	F6257-1868	99.92
237	F5893-0125	99.91
238	F5001-0908	99.91
239	T6004352	99.91
240	F2580-0215	99.88

Table S3 – Continued from previous page

	Molecule Name	Percentage G2/M normalized to Taxol
241	F2506-1204	99.87
242	T5700556	99.86
243	5398404	99.82
244	F3406-4685	99.81
245	T6092746	99.80
246	F2509-0012	99.76
247	ASN 05545569	99.62
248	F1298-0314	99.61
249	5216136	99.59
250	ASN 01516512	99.58
251	5705516	99.55
252	F1414-1214	99.52
253	T6053947	99.47
254	5113188	99.46
255	F6225-0846	99.43
256	T5851166	99.38
257	5261528	99.37
258	F0652-0156	99.30
259	F1447-0190	99.29
260	F2873-0019	99.27
261	F3166-0515	99.27
262	5326500	99.27
263	F0672-0185	99.26
264	5310667	99.21
265	ASN 04371174	99.16
266	AST 5587907	99.13
267	ASN 05546059	98.99
268	5376280	98.98
269	T6062428	98.95
270	ASN 05940059	98.93
271	F1787-0617	98.88
272	5319994	98.88
273	5301303	98.85
274	5647184	98.71
275	F2663-0021	98.69
276	T5807000	98.68
277	F5019-0656	98.67
278	F5834-0457	98.66
279	F2509-0041	98.57
280	F2873-0019	98.56

Table S3 – Continued from previous page

	Molecule Name	Percentage G2/M normalized to Taxol
281	T5834505	98.54
282	F2269-0042	98.50
283	ASN 04395043	98.49
284	5693521	98.43
285	ASN 03432489	98.37
286	Paclitaxel	98.35
287	F3369-0640	98.26
288	F2745-0284	98.24
289	F2964-3057	98.22
290	F5792-0668	98.22
291	F0725-0302	98.19
292	F2269-0181	98.14
293	T5887213	98.14
294	F6195-1743	98.12
295	F1298-0842	98.10
296	ASN 04394959	98.07
297	5308473	98.04
298	F2135-0681	97.92
299	F1298-0404	97.89
300	T6051768	97.88
301	F2902-0413	97.86
302	F2659-0008	97.80
303	5554099	97.75
304	ASN 05446600	97.73
305	5213777	97.72
306	F2964-2721	97.70
307	5720020	97.68
308	5334549	97.68
309	ASN 05113329	97.68
310	F5069-0056	97.66
311	F2964-3058	97.63
312	5323564	97.62
313	5252917	97.61
314	T6004806	97.59
315	ASN 03321946	97.53
316	F1590-0052	97.53
317	F2050-0045	97.53
318	F1420-0733	97.50
319	ASN 05446217	97.47
320	T5878385	97.47

Table S3 – Continued from previous page

	Molecule Name	Percentage G2/M normalized to Taxol
321	F0012-0288	97.43
322	ASN 04886943	97.42
323	F3225-8526	97.36
324	F5772-8457	97.36
325	ASN 02254675	97.35
326	F2382-0276	97.35
327	F5128-0293	97.31
328	F2509-0045	97.27
329	MS-1503373	97.23
330	ASN 02254695	97.21
331	F2478-0125	97.21
332	F2269-0019	97.21
333	F1943-0019	97.18
334	F0708-0273	97.15
335	F3244-0255	97.14
336	5346277	97.11
337	AST 5546340	97.10
338	T6077976	97.10
339	T5899065	97.09
340	F2580-0140	97.09
341	F0603-0329	97.04
342	F2745-0271	97.03
343	F2984-0002	97.01
344	F2493-3293	96.99
345	T6053176	96.98
346	F3382-3525	96.98
347	F2803-0008	96.97
348	6625551	96.84
349	F3398-1415	96.80
350	F1298-0835	96.76
351	F3398-1226	96.71
352	F2590-0084	96.67
353	T5794424	96.63
354	F5834-4224	96.63
355	F5001-1581	96.57
356	T5614678	96.48
357	AST 5588889	96.47
358	F1848-0122	96.47
359	5284587	96.43
360	F0415-0027	96.40

Table S3 – Continued from previous page

	Molecule Name	Percentage G2/M normalized to Taxol
361	ASN 05443761	96.37
362	5552857	96.37
363	ASN 05543939	96.36
364	5679818	96.32
365	F0882-0730	96.27
366	T5793172	96.13
367	5378429	96.06
368	5316284	96.05
369	F6195-5748	96.04
370	F2743-0331	96.04
371	T6145342	96.03
372	ASN 05546061	96.00
373	MS-1800067	95.97
374	ASN 04394978	95.97
375	F3406-9688	95.96
376	F2580-0290	95.93
377	AST 5588336	95.83
378	F1858-0207	95.73
379	ASN 05546205	95.69
380	T6114925	95.69
381	F2269-0200	95.67
382	T6053386	95.52
383	F2580-0328	95.49
384	5240458	95.39
385	F5103-0059	95.35
386	F6195-5796	95.31
387	ASN 04371229	95.30
388	F3222-3467	95.21
389	T5869460	95.06
390	F0405-0785	95.04
391	5378172	95.03
392	MS-1500611	94.98
393	F3223-0079	94.97
394	T5758223	94.85
395	F5099-0676	94.85
396	F3398-0931	94.65
397	T6040301	94.64
398	6624472	94.61
399	AST 5588302	94.59
400	5623661	94.55

Table S3 – Continued from previous page

	Molecule Name	Percentage G2/M normalized to Taxol
401	F2269-0030	94.54
402	F3260-0795	94.49
403	F0651-0070	94.45
404	F1822-0560	94.40
405	5350849	94.31
406	T5687909	94.26
407	5547270	94.06
408	5566411	94.05
409	T5836001	93.99
410	F0012-0273	93.96
411	6617574	93.89
412	T6099168	93.81
413	T6042114	93.79
414	F1590-0060	93.66
415	F3398-1873	93.57
416	F3407-2408	93.26
417	SAM001246685	93.21
418	F3260-0797	93.10
419	T5981263	92.92
420	F3398-1411	92.87
421	F0526-1839	92.68
422	T6075414	92.52
423	5457379	92.48
424	F2580-0253	92.41
425	F0012-0270	92.25
426	F1298-0841	92.18
427	F3225-8556	92.16
428	ASN 04371230	91.98
429	F3407-0390	91.94
430	F1589-0206	91.75
431	F1298-0922	91.59
432	F2701-1288	91.45
433	ASN 05443933	90.93
434	F2964-2693	90.91
435	F1385-0098	90.84
436	AST 5588397	90.80
437	5467203	90.74
438	ASN 05107027	90.72
439	T5821395	90.64
440	F0882-0694	90.60

Table S3 – Continued from previous page

	Molecule Name	Percentage G2/M normalized to Taxol
441	F3406-4698	90.44
442	F3385-3661	90.38
443	F2063-0217	90.30
444	5278450	90.27
445	F1590-0057	90.24
446	AST 5940128	90.22
447	F1155-0342	90.21
448	F0453-0145	89.66
449	T6023589	89.44
450	F5086-0273	89.18
451	F3407-2398	88.78
452	ASN 05113199	88.35
453	5661863	88.03
454	T5654678	87.93
455	F5897-0255	87.86
456	5213772	87.82
457	T5942300	87.63
458	F0651-0194	87.45
459	5543266	87.19
460	F2770-0080	86.99
461	F1593-0033	86.59
462	MS-200013	86.44
463	F0376-0324	86.44
464	F5858-0090	86.37
465	F5607-0070	86.21
466	F3382-7420	86.09
467	5480160	86.08
468	F2768-0361	85.96
469	F2833-0090	85.85
470	ASN 05543441	85.83
471	F5897-0217	85.75
472	F1191-0159	85.66
473	T5788025	85.17
474	F3406-9670	85.13
475	F0777-2455	85.11
476	ASN 09858411	84.94
477	F3406-4694	84.81
478	F6195-2759	84.63
479	5269674	84.56
480	F3398-1227	84.28

Table S3 – Continued from previous page

	Molecule Name	Percentage G2/M normalized to Taxol
481	F3283-0300	84.11
482	F5897-0217	84.04
483	F0666-0040	83.98

Table S4 – G1/S Chemical similarity network analysis pulldown (CSNAP)

Compound	Sum	Predicted Target
O00329	1	
O09028	2	
O14746	1	
O42275	2	
O50979	1	
O69002	1	
O70536	1	
O75908	1	
O94806	6	PRKD3
P00374	3	
P00734	26	F2 (Prothrombin)
P00742	6	F10
P00749	1	
P00766	23	Chymotrypsinogen
P04370	1	
P04626	1	
P05129	6	PRKCG
P05186	2	
P05771	6	PRKCB
P07900	1	
P08069	1	
P08246	25	ELANE
P08253	9	MMP2
P08581	3	
P08659	1	
P08842	1	
P09237	9	MMP7
P0AEK4	2	
P10415	4	
P10636	4	
P11412	4	
P11940	1	
P12268	1	
P12276	2	
P15431	2	
P15840	1	
P17252	6	PRKCA
P18054	5	
P18506	2	
P18508	2	

Table S4 – Continued from previous page

Compound	Sum	Predicted Target
P19969	2	
P20236	2	
P22303	1	
P23219	1	
P23574	2	
P23576	2	
P24723	6	PRKCH
P25101	1	
P25779	2	
P25963	5	
P26358	1	
P27540	1	
P28471	2	
P28473	2	
P30191	2	
P35354	1	
P35610	1	
P37231	1	
P41743	3	
P42337	1	
P42338	1	
P47989	2	
P48449	1	
P49327	1	
P50281	9	MMP14
P50579	2	
P52020	2	
P52209	4	
P53582	2	
P55789	1	
P56817	5	
P62813	2	
P63079	2	
P63138	2	
P81908	1	
Q02156	6	PRKCE
Q04206	5	
Q04759	6	PRKCQ
Q05513	3	
Q05655	6	PRKCD

Table S4 – Continued from previous page

Compound	Sum	Predicted Target
Q12809	1	
Q13093	1	
Q13627	1	
Q15056	1	
Q15139	6	PRKD1
Q15788	1	
Q16539	2	
Q16665	1	
Q27757	1	
Q72547	16	
Q72874	7	
Q7ZJM1	1	
Q8NER1	2	
Q91ZM7	2	
Q965D5	4	
Q965D6	4	
Q965D7	4	
Q9ES14	2	
Q9XUB2	1	

Table S5 – G2/M Chemical similarity network analysis pulldown (CSNAP)

Compound	Sum	Predicted Target
A3EZI9	2	
O00141	37	
O00329	37	
O00418	11	
O00444	11	
O00506	11	
O00519	3	
O00767	155	SCD
O09028	1	
O14733	11	
O14746	1	
O14757	41	
O14920	37	
O14965	48	ARUKA
O14976	11	
O15111	37	
O15146	48	MUSK
O15245	6	
O15264	37	
O15530	11	
O42275	16	
O43293	22	
O43318	11	
O43353	22	
O43741	11	
O43924	12	
O60285	37	
O60563	11	
O60674	48	JAK2
O75116	39	
O75582	48	RPS6KA5
O75676	48	RPS6KA4
O75716	11	
O75914	48	PAK3
O76074	26	
O94768	11	
O94804	48	STK10
O94806	37	
O95067	11	
O95819	48	MAP4K4

Table S5 – Continued from previous page

Compound	Sum	Predicted Target
O95864	74	FADS2
O96013	24	
O96017	37	
O96020	22	
P00519	81	ABL1
P00533	52	EGFR
P00591	1	
P00742	2	
P00747	10	
P00761	2	
P00811	2	
P02550	46	TUBA1A
P02554	24	
P02766	4	
P02829	1	
P03118	2	
P03120	2	
P03372	8	
P03905	5	
P04015	2	
P04049	56	RAF1
P04150	2	
P04350	108	TUBB4A
P04626	50	ERBB1
P04629	48	NTRK1
P04637	5	
P04925	7	
P05106	4	
P05129	37	
P05186	5	
P05412	1	
P05771	48	PRKCB
P05979	9	
P06213	51	INSR
P06239	48	LCK
P06241	50	FYN
P06276	26	
P06401	1	
P06493	49	CDK1
P06536	1	

Table S5 – Continued from previous page

Compound	Sum	Predicted Target
P06756	4	
P07332	48	FES
P07333	48	CSF1R
P07437	110	TUBB
P07900	5	
P07947	48	YES1
P07948	48	LYN
P07949	48	RET
P08069	48	IGF1R
P08173	2	
P08183	12	
P08238	1	
P08246	10	
P08575	8	
P08581	48	MET
P08631	48	HCK
P08659	50	
P08684	4	
P08908	2	
P08922	48	ROS1
P09619	48	PDGFRB
P09769	48	FGR
P0AE18	4	
P0C6U8	6	
P10636	22	
P10721	48	KIT
P10845	2	
P11309	48	PIM1
P11362	50	FGFR1
P11387	3	
P11388	34	
P11712	2	
P11802	37	
P11926	2	
P12530	2	
P12931	50	SRC
P13516	155	SCD1
P14061	17	
P14416	8	
P14616	48	INSRR

Table S5 – Continued from previous page

Compound	Sum	Predicted Target
P14635	11	
P15056	48	BRAF
P15108	3	
P15207	1	
P15374	4	
P15431	1	
P15735	48	PHKG2
P15823	3	
P16234	48	PDGFRA
P16257	6	
P16499	12	
P16591	48	FER
P16885	10	
P17252	50	PRKCA
P17612	37	
P17948	48	FLT1
P18031	1	
P18130	1	
P18506	1	
P18508	1	
P18545	12	
P19020	3	
P19327	3	
P19784	35	
P19969	1	
P20236	1	
P20248	11	
P21396	3	
P21397	3	
P21452	4	
P21554	5	
P21709	24	
P21802	48	FGFR2
P21917	5	
P21980	2	
P22199	1	
P22303	28	
P22455	48	FGFR4
P22607	48	FGFR3
P23141	26	

Table S5 – Continued from previous page

Compound	Sum	Predicted Target
P23415	2	
P23416	2	
P23443	37	
P23458	48	JAK1
P23528	1	
P23574	1	
P23576	1	
P23944	3	
P24557	2	
P24666	48	ACP1
P24723	37	
P24864	25	
P24941	75	CDK2
P25103	3	
P25708	1	
P25779	8	
P27338	5	
P27361	48	MAPK3
P27448	37	
P27652	37	
P27695	40	
P27815	2	
P28223	1	
P28272	1	
P28335	4	
P28471	1	
P28473	1	
P28482	88	MAPK1
P29274	5	
P29317	48	EPHA2
P29320	48	EPHA3
P29322	22	
P29323	48	EPHB2
P29350	1	
P29376	48	LTK
P29597	48	TYK2
P30082	1	
P30083	125	Vipr1
P30191	1	
P30281	11	

Table S5 – Continued from previous page

Compound	Sum	Predicted Target
P30304	2	
P30418	6	
P30530	48	AXL
P31645	2	
P31652	1	
P31749	50	AKT1
P31751	48	AKT2
P32238	2	
P33032	2	
P33261	3	
P33527	2	
P33533	1	
P33535	1	
P33981	48	TTK
P34947	11	
P34969	1	
P34972	5	
P34975	1	
P35236	48	PTPN7
P35354	2	
P35398	1	
P35462	2	
P35557	15	
P35913	12	
P35916	48	FLT4
P35961	3	
P35968	52	KDR
P36888	57	FLT3
P36894	11	
P36896	22	
P36897	24	
P37023	11	
P37059	17	
P40925	2	
P41143	2	
P41240	48	CSK
P41743	37	
P42336	37	
P42345	23	
P42574	2	

Table S5 – Continued from previous page

Compound	Sum	Predicted Target
P42680	37	
P42681	48	TEC
P42684	48	ABL2
P42685	48	FRK
P43140	3	
P43250	37	
P43403	48	ZAP70
P43405	37	
P45983	100	MAPK8
P45984	68	MAPK9
P47199	1	
P47871	27	
P48729	48	CSN1A1
P48730	22	
P49137	37	

Table S6 – Potency and phenotypic data

Compound ID	Molecule Name	Normalized G2/M arrest	Cell Viability IC_{50} (μM)	Phenotype class
1	F2093-0051	117.41 ± 5.07	2.18	Non-mitotic
2	F1298-0926	113.81 ± 1.20	0.75	Mixed
3	F2487-0352	110.54 ± 2.18	1.03	Multipolar, Depolymerizer
4	F2481-0446	110.20 ± 0.34	0.89	Depolymerizer
5	F1015-0297	109.90 ± 3.94	0.67	Depolymerizer
6	F0193-0287	109.75 ± 5.87	1.02	Mixed
7	F3225-8496	109.71 ± 0.62	0.49	Depolymerizer
8	F0187-0071	109.60 ± 3.65	1.89	Depolymerizer
9	F2269-0014	109.50 ± 0.64	1.02	Depolymerizer
10	F6195-5713	109.14 ± 0.72	1.24	Depolymerizer
11	F1848-0114	109.04 ± 2.11	0.21	Strong Depolymerizer
12	F2506-1309	108.97 ± 1.24	1.27	Multipolar, Depolymerizer
13	F2211-0050	108.85 ± 0.06	1.19	Depolymerizer
14	F2503-0097	108.81 ± 0.53	0.91	Depolymerizer
15	F5871-3531	107.09 ± 1.84	3.77	Mixed
16	F2616-0891	106.23 ± 5.16	0.31	Depolymerizer
17	F2487-0240	105.99 ± 2.79	0.86	Depolymerizer
18	F3406-4686	105.91 ± 1.84	0.10	Depolymerizer
19	F3398-5051	105.40 ± 1.89	0.89	Depolymerizer
20	F3406-0765	105.31 ± 1.42	0.58	Depolymerizer
21	F0280-0213	105.28 ± 3.42	2.16	Depolymerizer
22	F3406-4697	105.19 ± 0.36	0.05	Strong Depolymerizer
23	F6195-2790	105.09 ± 4.15	0.54	Depolymerizer
24	ASN 05397535	105.08 ± 0.94	N/A	N/A
25	F2158-0029	103.83 ± 1.09	8.61	Non-mitotic
26	F3379-0117	103.50 ± 3.78	0.81	Depolymerizer
27	F3222-4636	103.40 ± 0.27	2.95	Depolymerizer
28	F6195-2957	103.39 ± 1.86	0.28	Depolymerizer
29	F3406-5077	103.13 ± 1.01	0.17	Depolymerizer
30	F3406-1010	102.54 ± 2.73	0.09	Strong Depolymerizer
31	F3406-5050	101.27 ± 2.99	1.42	Multipolar, Depolymerizer
32	F3406-0773	101.26 ± 4.15	0.49	Multipolar, Depolymerizer
33	5262045	101.22 ± 4.19	0.88	Depolymerizer
34	T5730868	100.82 ± 4.10	0.72	Depolymerizer, Unaligned
35	F3406-5142	100.16 ± 4.32	0.25	Depolymerizer
36	F5228-1317	99.98 ± 3.68	0.37	Depolymerizer
37	T5700556	99.86 ± 2.46	1.71	Non-mitotic

Table S6 – Continued from previous page

Compound ID	Molecule Name	Normalized G2/M arrest	Cell Viability IC_{50} (μM)	Phenotype class
38	5398404	99.82 ± 2.52	1.71	Depolymerizer
39	T6092746	99.80 ± 2.00	0.51	Depolymerizer
40	T6053947	99.47 ± 0.58	0.28	Depolymerizer
41	F3166-0515	99.27 ± 1.45	1.05	Depolymerizer
42	F6195-1743	98.12 ± 3.34	0.87	Depolymerizer
43	F2902-0413	97.86 ± 7.80	0.52	Depolymerizer
44	F5772-8457	97.36 ± 2.83	1.21	Depolymerizer
45	T6077976	97.10 ± 2.36	4.11	Depolymerizer
46	T6145342	96.03 ± 7.12	3.49	Depolymerizer
47	F5103-0059	95.35 ± 1.29	0.61	Depolymerizer
48	F3223-0079	94.97 ± 2.02	34.30	Depolymerizer
49	T6040301	94.64 ± 2.17	1.52	Depolymerizer
50	F3407-0390	91.94 ± 1.34	1.11	Depolymerizer
51	ASN 05107027	90.72 ± 4.40	3.03	Depolymerizer
52	T5942300	87.63 ± 5.10	3.84	Depolymerizer
53	F5607-0070	86.21 ± 4.75	1.71	Depolymerizer

Figure S7 – Cell viability IC_{50} panel of cell lines

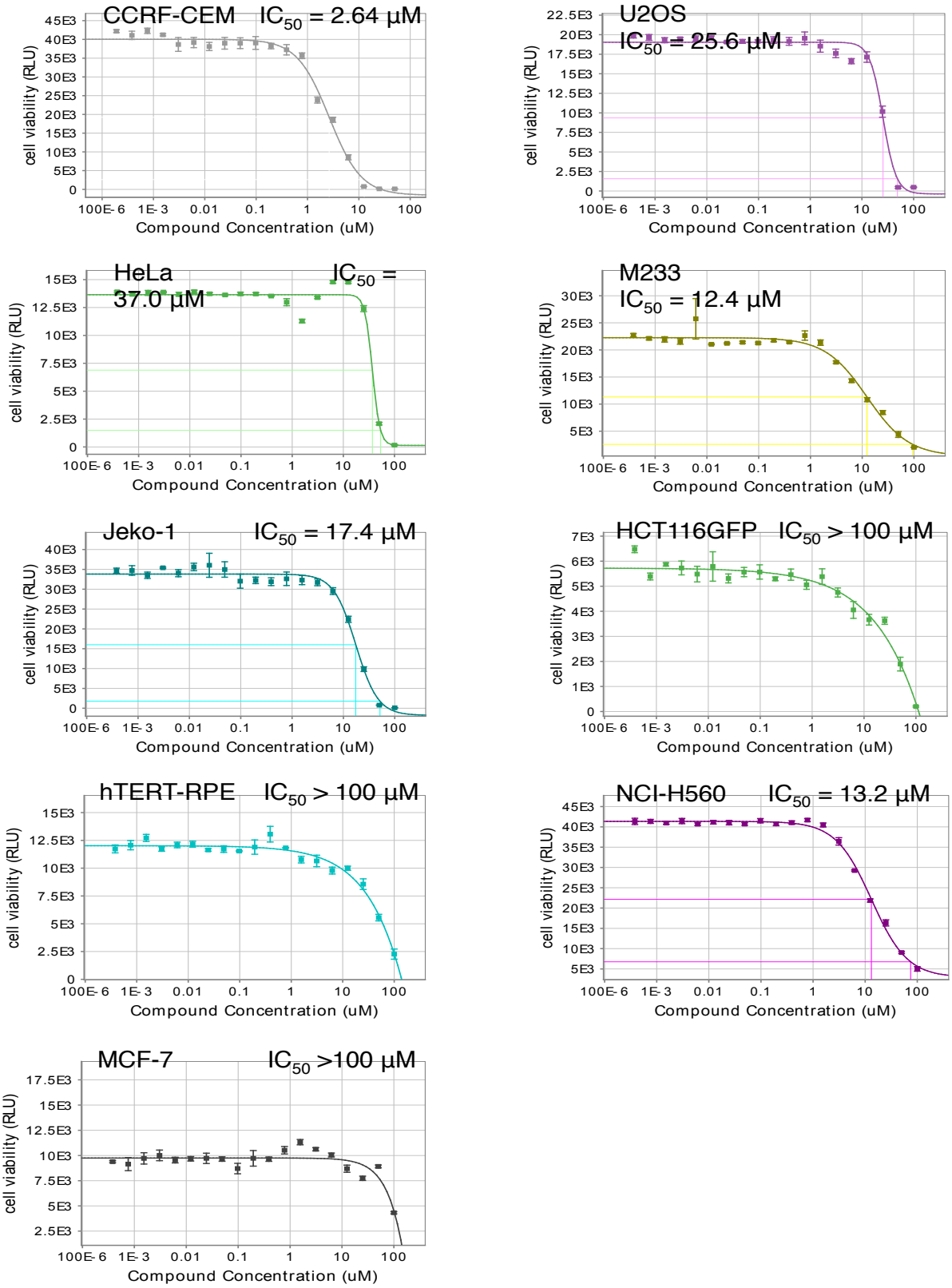

Figure S8 – Cell viability IC_{50} panel of leukemia cell lines

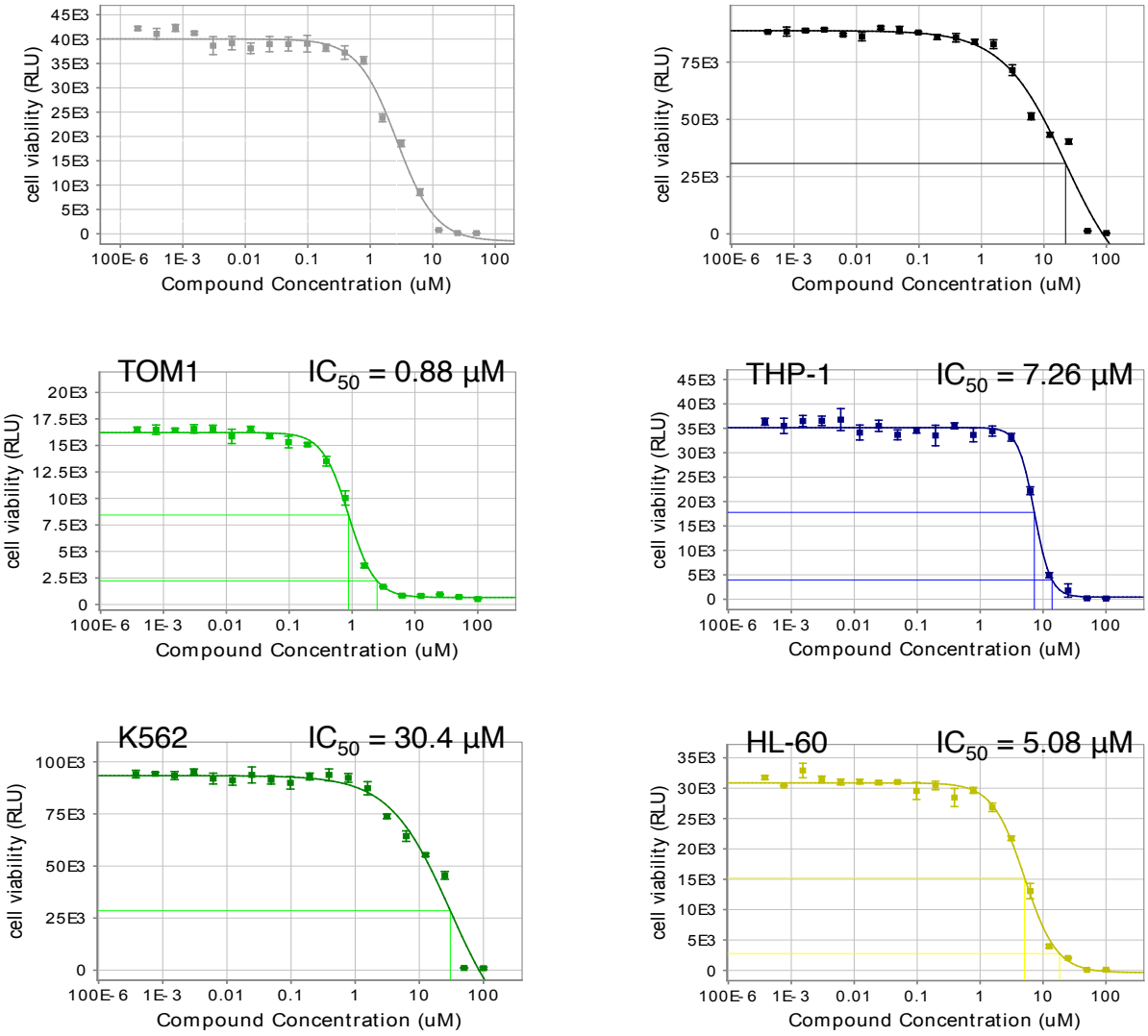

CHAPTER 9 – REFERENCES

1. De Baere, I., et al., *Purification of porcine brain protein phosphatase 2A leucine carboxyl methyltransferase and cloning of the human homologue.* Biochemistry, 1999. **38**(50): p. 16539-47.
2. Virshup, D.M. and S. Shenolikar, *From promiscuity to precision: protein phosphatases get a makeover.* Mol Cell, 2009. **33**(5): p. 537-45.
3. Sents, W., et al., *The biogenesis of active protein phosphatase 2A holoenzymes: a tightly regulated process creating phosphatase specificity.* FEBS J, 2013. **280**(2): p. 644-61.
4. Longin, S., et al., *Selection of protein phosphatase 2A regulatory subunits is mediated by the C terminus of the catalytic Subunit.* J Biol Chem, 2007. **282**(37): p. 26971-80.
5. Ogris, E., et al., *A protein phosphatase methylesterase (PME-1) is one of several novel proteins stably associating with two inactive mutants of protein phosphatase 2A.* J Biol Chem, 1999. **274**(20): p. 14382-91.
6. Xing, Y., et al., *Structural mechanism of demethylation and inactivation of protein phosphatase 2A.* Cell, 2008. **133**(1): p. 154-63.
7. Lee, J.A. and D.C. Pallas, *Leucine carboxyl methyltransferase-1 is necessary for normal progression through mitosis in mammalian cells.* J Biol Chem, 2007. **282**(42): p. 30974-84.
8. Ortega-Gutierrez, S., et al., *Targeted disruption of the PME-1 gene causes loss of demethylated PP2A and perinatal lethality in mice.* PLoS One, 2008. **3**(7): p. e2486.
9. Puustinen, P., et al., *PME-1 protects extracellular signal-regulated kinase pathway activity from protein phosphatase 2A-mediated inactivation in human malignant glioma.* Cancer Res, 2009. **69**(7): p. 2870-7.
10. Bachovchin, D.A., et al., *Academic cross-fertilization by public screening yields a remarkable class of protein phosphatase methylesterase-1 inhibitors.* Proc Natl Acad Sci U S A, 2011. **108**(17): p. 6811-6.
11. Bachovchin, D.A., et al., *Discovery and optimization of sulfonyl acrylonitriles as selective, covalent inhibitors of protein phosphatase methylesterase-1.* J Med Chem, 2011. **54**(14): p. 5229-36.
12. Torres, J.Z., J.J. Miller, and P.K. Jackson, *High-throughput generation of tagged stable cell lines for proteomic analysis.* Proteomics, 2009. **9**(10): p. 2888-91.
13. Torres, J.Z., K.H. Ban, and P.K. Jackson, *A Specific Form of Phospho Protein Phosphatase 2 Regulates Anaphase-promoting Complex/Cyclosome Association with Spindle Poles.* Mol Biol Cell, 2010. **21**(6): p. 897-904.
14. Wurzenberger, C. and D.W. Gerlich, *Phosphatases: providing safe passage through mitotic exit.* Nat Rev Mol Cell Biol, 2011. **12**(8): p. 469-82.
15. Barr, F.A., P.R. Elliott, and U. Gruneberg, *Protein phosphatases and the regulation of mitosis.* J Cell Sci, 2011. **124**(Pt 14): p. 2323-34.
16. Funabiki, H. and D.J. Wynne, *Making an effective switch at the kinetochore by phosphorylation and dephosphorylation.* Chromosoma, 2013. **122**(3): p. 135-58.
17. Sontag, E., et al., *Altered expression levels of the protein phosphatase 2A ABalphaC enzyme are associated with Alzheimer disease pathology.* J Neuropathol Exp Neurol, 2004. **63**(4): p. 287-301.

18. Sontag, E., et al., *Molecular interactions among protein phosphatase 2A, tau, and microtubules. Implications for the regulation of tau phosphorylation and the development of tauopathies.* J Biol Chem, 1999. **274**(36): p. 25490-8.
19. Foley, E.A. and T.M. Kapoor, *Microtubule attachment and spindle assembly checkpoint signalling at the kinetochore.* Nat Rev Mol Cell Biol, 2013. **14**(1): p. 25-37.
20. Chen, F., et al., *Multiple protein phosphatases are required for mitosis in Drosophila.* Curr Biol, 2007. **17**(4): p. 293-303.
21. Sawin, K.E., et al., *Mitotic spindle organization by a plus-end-directed microtubule motor.* Nature, 1992. **359**(6395): p. 540-3.
22. Reber, S.B., et al., *XMAP215 activity sets spindle length by controlling the total mass of spindle microtubules.* Nat Cell Biol, 2013. **15**(9): p. 1116-22.
23. Su, X., et al., *Microtubule-sliding activity of a kinesin-8 promotes spindle assembly and spindle-length control.* Nat Cell Biol, 2013. **15**(8): p. 948-57.
24. Loughlin, R., et al., *Katanin contributes to interspecies spindle length scaling in Xenopus.* Cell, 2011. **147**(6): p. 1397-407.
25. Goshima, G. and J.M. Scholey, *Control of mitotic spindle length.* Annu Rev Cell Dev Biol, 2010. **26**: p. 21-57.
26. Torres, J.Z., et al., *The STARD9/Kif16a Kinesin Associates with Mitotic Microtubules and Regulates Spindle Pole Assembly.* Cell, 2011. **147**(6): p. 1309-23.
27. Senese, S., et al., *A unique insertion in STARD9's motor domain regulates its stability.* Mol Biol Cell, 2015. **26**(3): p. 440-52.
28. Senese, S., et al., *Chemical dissection of the cell cycle: probes for cell biology and anti-cancer drug development.* Cell Death Dis, 2014. **5**: p. e1462.
29. Pui, C.H. and S. Jeha, *New therapeutic strategies for the treatment of acute lymphoblastic leukaemia.* Nat Rev Drug Discov, 2007. **6**(2): p. 149-65.
30. Pui, C.-H. and W.E. Evans, *A 50-Year Journey to Cure Childhood Acute Lymphoblastic Leukemia.* Seminars in Hematology, 2013. **50**(3): p. 185-196.
31. Wei, M.C. and M.L. Cleary, *Novel methods and approaches to acute lymphoblastic leukemia drug discovery.* Expert Opinion on Drug Discovery, 2014. **9**(12): p. 1435-1446.
32. Vagace, J.M., et al., *Central nervous system chemotoxicity during treatment of pediatric acute lymphoblastic leukemia/lymphoma.* Crit Rev Oncol Hematol, 2012.
33. Shaffer, B.C., et al., *Drug resistance: Still a daunting challenge to the successful treatment of AML.* Drug Resist Updat, 2012. **15**(1-2): p. 62-9.
34. Woessner, D.W., C.S. Lim, and M.W. Deininger, *Development of an effective therapy for chronic myelogenous leukemia.* Cancer J, 2011. **17**(6): p. 477-86.
35. Wierda, W.G., et al., *Chronic lymphocytic leukemia: new concepts for future therapy.* Clin Lymphoma Myeloma Leuk, 2010. **10**(5): p. 369-78.
36. van der Plas E, N.B., Butcher DT, Hitzler JK, Weksberg R, Ito S, Schachar R., *Neurocognitive Late Effects of Chemotherapy in Survivors of Acute Lymphoblastic Leukemia: Focus on Methotrexate.* J Can Acad Child Adolesc Psychiatry, 2015. **24**(1): p. 25-32.
37. Sathiapalan RK, E.-S.H., *Enhanced vincristine neurotoxicity from drug interactions: case report and review of literature.* Pediatr Hematol Oncol, 2001. **18**(8): p. 543-6.
38. Jabbour, E.e.a., *Neurological complications associated with intrathecal liposomal cytarabine given prophylactically in combination with high dose methotrexate and cytarabine to patients with acute lymphocytic leukemia.* Blood, 2007. **5**.

39. Consoli U, P.W., Ling YH, Mahadevia R, Griffin M, Zhao S, Perez-Soler R, Andreeff M, *The novel anthracycline annamycin is not affected by P-glycoprotein-related multidrug resistance: comparison with idarubicin and doxorubicin in HL-60 leukemia cell lines.* Blood, 1996. **88**(2): p. 633-44.
40. J, W., *From methotrexate to pemetrexed and beyond. A review of the pharmacodynamic and clinical properties of antifolates.* Invest New Drugs, 2006. **24**(1): p. 37-77.
41. Zou Y, P.W., Stephens LC, Perez-Soler R, *Preclinical toxicity of liposome-incorporated annamycin: selective bone marrow toxicity with lack of cardiotoxicity.* Clin Cancer Res, 1995. **1**(11): p. 1369-74.
42. Boman, N.L., Bally, M. B., Cullis, P. R., Mayer, L. D. & Webb, M. S, *Encapsulation of vincristine in liposomes reduces its toxicity and improves its antitumor efficacy.* J, Liposome Res, 1995. **5**: p. 523-41.
43. Gelmon KA, T.A., Diab AR, Bally MB, Embree L, Hudon N, Dedhar C, Ayers D, Eisen A, Melosky B, Burge C, Logan P, Mayer LD, *Phase I study of liposomal vincristine.* J Clin Oncol, 1999. **17**(2): p. 697-705.
44. Thomas DA, S.A., Cortes J, Faderl S, O'Brien S, Giles FJ, Garcia-Manero G, Rodriguez MA, Cabanillas F, Kantarjian H, *Phase II study of sphingosomal vincristine in patients with recurrent or refractory adult acute lymphocytic leukemia.* Cancer, 2006. **06**(1): p. 120-7.
45. Iacobucci, I., et al., *Cytogenetic and molecular predictors of outcome in acute lymphocytic leukemia: recent developments.* Curr Hematol Malig Rep, 2012. **7**(2): p. 133-43.
46. Kristensen, V.N., et al., *Principles and methods of integrative genomic analyses in cancer.* Nat Rev Cancer, 2014. **14**(5): p. 299-313.
47. Martell, R.E., et al., *Discovery of novel drugs for promising targets.* Clin Ther, 2013. **35**(9): p. 1271-81.
48. Cong, F., A.K. Cheung, and S.M. Huang, *Chemical genetics-based target identification in drug discovery.* Annu Rev Pharmacol Toxicol, 2012. **52**: p. 57-78.
49. McDermott, S.P., et al., *A small molecule screening strategy with validation on human leukemia stem cells uncovers the therapeutic efficacy of kinetin riboside.* Blood, 2012. **119**(5): p. 1200-7.
50. Gasparetto, M., et al., *Identification of compounds that enhance the anti-lymphoma activity of rituximab using flow cytometric high-content screening.* J Immunol Methods, 2004. **292**(1-2): p. 59-71.
51. Rix, U. and G. Superti-Furga, *Target profiling of small molecules by chemical proteomics.* Nat Chem Biol, 2009. **5**(9): p. 616-24.
52. Dillman R.O., D.R.B., Green M.R., Weiss R.B., Gottlieb A.J., Caplan S., Kopel S., Preisler H., McIntyre O.R., Schiffer C, *A comparative study of two different doses of cytarabine for acute myeloid leukemia: A phase III trial of Cancer and Leukemia Group B.* Blood, 1991. **78**: p. 2520-2526.
53. Salazar-Mendiguchía, J., et al., *Anthracycline-mediated cardiomyopathy: Basic molecular knowledge for the cardiologist.* Archivos de Cardiología de México, 2014. **84**(3): p. 218-223.
54. Broxterman HJ, G.K., Verheul HM, *Understanding the causes of multidrug resistance in cancer: a comparison of doxorubicin and sunitinib.* Drug Resist Updat, 2009. **12**(4-5): p. 114-26.

55. Lo, Y.-C., et al., *Large-Scale Chemical Similarity Networks for Target Profiling of Compounds Identified in Cell-Based Chemical Screens.* PLOS Computational Biology, 2015. **11**(3): p. e1004153.
56. Hendzel, M.J., et al., *Mitosis-specific phosphorylation of histone H3 initiates primarily within pericentromeric heterochromatin during G2 and spreads in an ordered fashion coincident with mitotic chromosome condensation.* Chromosoma, 1997. **106**(6): p. 348-60.
57. Chowdhury, I., B. Tharakan, and G.K. Bhat, *Caspases - an update.* Comp Biochem Physiol B Biochem Mol Biol, 2008. **151**(1): p. 10-27.
58. Napper, A.D. and V.G. Watson, *Targeted drug discovery for pediatric leukemia.* Front Oncol, 2013. **3**: p. 170.
59. Lomenick B, H.R., Jonai N, Chin RM, Aghajan M, Warburton S, Wang J, Wu RP, Gomez F, Loo JA, Wohlschlegel JA, Vondriska TM, Pelletier J, Herschman HR, Clardy J, Clarke CF, Huang J., *Target identification using drug affinity responsive target stability (DARTS).* Proc Natl Acad Sci USA, 2009. **106**(51): p. 21984-9.
60. Chelius D, B.P., *Quantitative profiling of proteins in complex mixtures using liquid chromatography and mass spectrometry.* J Proteome Res, 2002. **1**(4): p. 317-23.
61. Asara JM, C.H., Freimark LM, Cantley LC, *A label-free quantification method by MS/MS TIC compared to SILAC and spectral counting in a proteomics screen.* Proteomics, 2008. **8**(5): p. 994-9.
62. Pierce MM, R.C., Nall BT, *Isothermal Titration Calorimetry of Protein–Protein Interactions.* Methods, 1999. **19**(2): p. 213-21.
63. Lomenick B, O.R., Huang J, *Identification of Direct Protein Targets of Small Molecules.* ACS Chem Biol, 2011. **6**(1): p. 34-46.
64. Drouin, L., et al., *Structure Enabled Design of BAZ2-ICR, A Chemical Probe Targeting the Bromodomains of BAZ2A and BAZ2B.* Journal of Medicinal Chemistry, 2015. **58**(5): p. 2553-2559.
65. Tang, C.-H.A., et al., *Inhibition of ER stress–associated IRE-1/XBP-1 pathway reduces leukemic cell survival.* Journal of Clinical Investigation, 2014. **124**(6): p. 2585-2598.
66. Calfon, M., H.Zeng,F.Urano,J.H.Till,S.R.Hubbard,H.P.Harding,S.G. Clark, and D. Ron, *IRE1 couples endoplasmic reticulum load to secretory capacity by processing the XBP-1 mRNA.* Nature, 2002. **415**: p. 92-96.
67. Yoshida, H., T. Matsui, A. Yamamoto, T. Okada, and K. Mori, *XBP1 mRNA is induced by ATF6 and spliced by IRE1 in response to ER stress to produce a highly active transcription factor.* Cell, 2001. **107**: p. 881-891.
68. Lee, A.H., N.N. Iwakoshi, and L.H. Glimcher, *XBP-1 Regulates a Subset of Endoplasmic Reticulum Resident Chaperone Genes in the Unfolded Protein Response.* Molecular and Cellular Biology, 2003. **23**(21): p. 7448-7459.
69. Muller, S.F., P.; Knapp, S, *Brommodomains as Therapeutic Targets.* Expert Rev Mol Med, 2011. **13**: p. e29.
70. Filippakopoulos, P.K., S, *Targeting Bromodomains: Epigenetic Readers of Lysine Acetylation.* Nature Rev. Drug Discovery, 2014(13): p. 337-356.
71. Chen, P., et al., *Discovery and Characterization of GSK2801, a Selective Chemical Probe for the Bromodomains BAZ2A and BAZ2B.* Journal of Medicinal Chemistry, 2015: p. 150418091209006.

72. McCarthy, M.I., et al., *Identification of a Sudden Cardiac Death Susceptibility Locus at 2q24.2 through Genome-Wide Association in European Ancestry Individuals.* PLoS Genetics, 2011. **7**(6): p. e1002158.
73. Strohner R, N.A., Jansa P, Hofmann-Rohrer U, Santoro R, Längst G, Grummt I, *NoRC-A Novel Member of Mammalian ISWI-Containing Chromatin Remodeling Machines.* EMBO J, 2001. **20**(17): p. 4892-900.
74. Mayer C, N.M., Grummt I, *The Structure of NoRC- Associated RNA is Crucial for Targeting the Chromatin Remodelling Complex NoRC to the Nucleus.* EMBO Rep, 2008. **9**(8): p. 774-80.
75. Gu L, F.S., Oakes CC, Simon R, Grupp K, Gerig CY, Bär D, Robinson MD, Baer C, Weiss M, Gu Z, Schapira M, Kuner R, Sültmann H, Provenzano M; ICGC Project on Early Onset Prostate Cancer, Yaspo ML, Brors B, Korbel J, Schlomm T, Sauter G, Eils R, Plass C, Santoro *BAZ2A (TIP5) is Involved in Epigenetic Alterations in Prostate Cancer and its Overexpression Predicts Disease Recurrence.* Nat Genet, 2015. **47**(1): p. 22-30.
76. Bassik MC, K.M., Lebbink RJ, Wang S, Hein MY, Poser I, Weibezahn J, Horlbeck MA, Chen S, Mann M, Hyman AA, Leproust EM, McManus MT, Weissman JS., *A systematic mammalian genetic interaction map reveals pathways underlying ricin suscep- tibility.* Cell, 2013. **152**(4): p. 909-22.
77. Matheny, Christina J., et al., *Next-Generation NAMPT Inhibitors Identified by Sequential High-Throughput Phenotypic Chemical and Functional Genomic Screens.* Chemistry & Biology, 2013. **20**(11): p. 1352-1363.
78. Chonghaile, T.N., et al., *Maturation Stage of T-cell Acute Lymphoblastic Leukemia Determines BCL-2 versus BCL-XL Dependence and Sensitivity to ABT-199.* Cancer Discovery, 2014. **4**(9): p. 1074-1087.
79. Senese, S., et al., *Chemical dissection of the cell cycle: probes for cell biology and anti-cancer drug development.* Cell Death and Disease, 2014. **5**(10): p. e1462.
80. Zhang, J.H., T.D. Chung, and K.R. Oldenburg, *A Simple Statistical Parameter for Use in Evaluation and Validation of High Throughput Screening Assays.* J Biomol Screen, 1999. **4**(2): p. 67-73.